



Sarah Dörschlag, BSc

# Development of zinc oxide nanostructures by plasma-enhanced atomic layer deposition

## MASTER'S THESIS

to achieve the university degree of

Diplom-Ingenieurin

Master's degree programme: Technical Physics

submitted to

**Graz University of Technology**

Supervisor

Ass.Prof. Dr. Anna Maria Coclite

Institute of Solid State Physics

## **AFFIDAVIT**

I declare that I have authored this thesis independently, that I have not used other than the declared sources/resources, and that I have explicitly indicated all material which has been quoted either literally or by content from the sources used. The text document uploaded to TUGRAZonline is identical to the present master's thesis.

---

Date

---

Signature

## ABSTRACT

---

Atomic Layer Deposition (ALD) of zinc oxide has become increasingly significant in recent research. Zinc oxide (ZnO), a wide band gap semiconductor, is beside its many applicabilities in optic, optoelectronics, UV-blocking systems and in medicine, with its semi-conducting and piezoelectric properties, a promising material as a pressure-sensing shell material for the ERC-granted project "Smart Core/Shell Nanorod Arrays for Artificial Skin".

In order to create nanostructured zinc oxide, a combination of ALD and lithographic techniques is needed. Plasma Enhanced Atomic Layer Deposition (PEALD) is a vapour phase thin film deposition technique, which has several advantages compared to other chemical deposition techniques. Thanks to the high reactivity of the plasma species, the deposition takes place at reduced processing temperature and provides as a result more freedom in processing conditions and material tuning. For the lithographic techniques a variation of the shadow mask lithography and electron beam lithography is used, followed by a lift-off step.

After the optimization of the ALD process with the appropriate condition parameters, first steps were taken in structuring ZnO by shadow mask lithography. To reach structures in the nanometer range, Electron Beam Lithography was consulted. After the lift-off, nanostructured ZnO could be obtained, although in an unpredictable shape.

During the integration process of nanostructuring ZnO, the growth of ZnO on polymers is also investigated, since they are an important component in the procedure of lithography. The results of several analysing methods, like ellipsometry, X-ray reflectivity and X-ray diffraction, show that in spite of the diffusion of ZnO into the polymer, high-quality, conformal zinc oxide with a preferential crystalline orientation is grown.



## KURZFASSUNG

---

Zinkoxid, ein Halbleiter mit einer direkten Bandlücke, eignet sich, neben seinen zahlreichen Anwendungen in den Bereichen der Optik, Optoelektronik, Sonnenschutz und in der Medizin, dank seiner guten piezoelektrischen Leitfähigkeit als druckempfindliches Hüllenmaterial in dem ERC-gesponserten Projekt "Smart Core/Shell Nanorod Arrays for Artificial Skin".

Um nanostrukturiertes Zinkoxid zu erhalten, wird eine Kombination aus Atomlagenabscheidung (Atomic Layer Deposition, ALD) und lithographischen Techniken benötigt.

Plasma-Atomlagenabscheidung (Plasma Enhanced Atomic Layer Deposition, PEALD) ist eine Technik, die mittels Plasma ein Beschichtungsverfahren bei niedrigen Temperaturen (Raumtemperatur) ermöglicht. Darüber hinaus bietet dieses Verfahren mehr Freiheit in der Einstellung verschiedenster Prozess- und Materialparameter.

Als lithographische Techniken dienen der Schablonendruck (Shadow Mask Lithography) und die Elektronenstrahlolithographie (Electron Beam Lithography).

Nachdem die Parameter für den ALD-Prozess optimiert wurden, konnten mittels Schablonendruck erste Versuche in der Strukturierung von ZnO vorgenommen werden. Um Formationen im Nanometerbereich zu erhalten, wurde die Elektronenstrahlolithographie hinzugezogen.

Nach dem Lift-Off konnte nanostrukturiertes ZnO gewonnen werden, wenn auch die Präzisierung der Form noch angepasst werden muss. Während des Prozesses der Nanostrukturierung des ZnO, wurde auch das Wachstum von ZnO auf Polymeren untersucht, da diese eine entscheidende Komponente in der Lithographie darstellen. Die Ergebnisse verschiedener Untersuchungsmethoden, wie Ellipsometrie, Röntgenreflektometrie und Röntgendiffraktometrie, zeigen, dass trotz einer Diffusion des ZnO in das Polymer, hochqualitative, gleichmäßige ZnO-Dünnschichten mit einer kristallinen Vorzugsrichtung erzeugt werden.



## ACKNOWLEDGMENTS

---

Firstly, I would like to express my sincere gratitude to my supervisor Prof. Anna Maria Coclite for her ever-present support and motivation throughout my thesis. I have been extremely lucky to have had a supervisor, who cared so much about my work, and who always responded to my questions so promptly. I would also like to thank Alberto Perrotta, who introduced me to the lab and offered his continuous advice during my work.

I am thankful to my colleagues Paul Christian, Marianne Kräuter, Fabian Muralter, Sebastian Peterka, Julian Pilz, Benjamin Sorgmann and Katrin Unger for the great working environment.

Thank you to Prof. Roland Resel and his group members, especially Stefan Pachmajer, for their help regarding x-ray measurements and constructive discussions during our pleasant group lunchtimes.

I would like to acknowledge Prof. Joachim Krenn and Prof. Andreas Hohenau from the University of Graz for their kind support and expertise with the electron beam lithography experiments. I would also like to thank Prof. Peter Hadley and Prof. Günter Leising for letting me use the SEM and the FTIR.

I am so grateful to the friends I met through my physics studies, who made this time in Graz precious.

Thank you, Philipp, for accompanying me through all the literal ups and downs during my thesis.

Finally, I want to thank my parents Anita and Ekki and my sister Kristin for their unconditional love, support and understanding as well as my best friend Vera. They were always there for me.



# CONTENTS

---

|            |  |           |
|------------|--|-----------|
| 1          | INTRODUCTION   | 1         |
| <b>I</b>   | <b>FUNDAMENTALS</b>                                      | <b>3</b>  |
| 2          | ATOMIC LAYER DEPOSITION                                  | 5         |
| 2.1        | Plasma Enhanced Atomic Layer Deposition . . . . .        | 6         |
| 3          | BASIC PROPERTIES OF ZINC OXIDE                           | 9         |
| 3.1        | Application of ZnO in Atomic Layer Deposition . . . . .  | 10        |
| 4          | LITHOGRAPHY  | 11        |
| 4.1        | Shadow Mask Lithography . . . . .                        | 11        |
| 4.1.1      | Polyvinyl alcohol . . . . .                              | 11        |
| 4.1.2      | Operating Principle . . . . .                            | 11        |
| 4.2        | Electron Beam Lithography . . . . .                      | 11        |
| 4.2.1      | Polymethyl methacrylate . . . . .                        | 11        |
| 4.2.2      | Operating principle . . . . .                            | 12        |
| 4.3        | Question of lift-off . . . . .                           | 12        |
| <b>II</b>  | <b>EXPERIMENTAL</b>                                      | <b>15</b> |
| 5          | SETUP AND RECIPE OPTIMIZATION                            | 17        |
| 5.1        | Setup . . . . .  | 17        |
| 5.2        | Recipe Optimization . . . . .                            | 19        |
| 5.2.1      | Procedure . . . . .                                      | 19        |
| 5.2.2      | Variation of precursor dose . . . . .                    | 20        |
| 5.2.3      | Variation of plasma dose . . . . .                       | 20        |
| 5.2.4      | Variation of purging time after precursor dose . . . . . | 20        |
| 5.2.5      | Variation of purging time after plasma dose . . . . .    | 21        |
| 5.2.6      | FTIR measurement . . . . .                               | 21        |
| 6          | SHADOW MASK LITHOGRAPHY                                  | 23        |
| 6.0.1      | Spincoating . . . . .                                    | 23        |
| 6.1        | Atomic Layer Deposition . . . . .                        | 23        |
| 6.2        | Lift off . . . . .                                       | 23        |
| 6.3        | Direct Lithography . . . . .                             | 24        |
| 7          | ELECTRON BEAM LITHOGRAPHY                                | 25        |
| 7.1        | Spincoating . . . . .                                    | 25        |
| 7.2        | Electron Beam Lithography . . . . .                      | 25        |
| 7.3        | Atomic Layer Deposition . . . . .                        | 25        |
| 7.4        | Lift-off . . . . .                                       | 26        |
| 8          | CHARACTERISATION TECHNIQUES                              | 27        |
| 8.1        | Spectroscopic ellipsometry (SE) . . . . .                | 27        |
| 8.2        | X-ray reflectivity . . . . .                             | 29        |
| <b>III</b> | <b>RESULTS AND DISCUSSION</b>                            | <b>33</b> |
| 9          | DETERMINATION OF THE OPTIMUM RECIPE                      | 35        |

|        |  |    |
|--------|--|----|
| 9.1    | Precursor dose . . . . .   | 35 |
| 9.1.1  | XRD measurements . . . . .   | 36 |
| 9.2    | Plasma dose . . . . .  | 36 |
| 9.3    | Purge after DEZ dose . . . . .   | 37 |
| 9.4    | Purge after plasma dose . . . . .                                      | 37 |
| 9.4.1  | XRD measurements . . . . .   | 38 |
| 9.5    | Optimum recipe . . . . .   | 40 |
| 9.5.1  | XRD measurements . . . . .   | 40 |
| 9.5.2  | FTIR measurement . . . . .   | 40 |
| 10     | SHADOW MASK LITHOGRAPHY . . . . .                                      | 43 |
| 10.1   | Analysis of the lift-off by optical microscopy . . . . .               | 43 |
| 10.2   | Spectroscopic ellipsometry of direct lithography sample . . . . .      | 43 |
| 11     | ELECTRON BEAM LITHOGRAPHY . . . . .                                    | 45 |
| 11.1   | Atomic Force Microscopy . . . . .                                      | 45 |
| 11.2   | Scanning Electron Microscopy . . . . .                                 | 46 |
| 11.3   | Examination of the lift-off . . . . .                                  | 46 |
| 12     | GROWTH OF ZINC OXIDE ON POLYMER . . . . .                              | 49 |
| 12.1   | Analysis of zinc oxide on PMMA by X-ray reflectivity . . . . .         | 49 |
| 12.2   | Analysis of zinc oxide on PMMA by spectroscopic ellipsometry . . . . . | 50 |
| 12.3   | Analysis of zinc oxide on PMMA by X-ray diffraction . . . . .          | 52 |
| 12.4   | Glass transition temperature measurements . . . . .                    | 54 |
| 12.4.1 | Comparison of PMMA and PMMA with ZnO on top . . . . .                  | 54 |
| 12.4.2 | Comparison of PMMA and plasma treated PMMA . . . . .                   | 55 |
| 13     | CONCLUSION AND OUTLOOK . . . . .                                       | 57 |
|        | BIBLIOGRAPHY . . . . .   | 59 |

## LIST OF FIGURES

---

|           |  |    |
|-----------|--|----|
| Figure 1  | Schematic of the process obtaining "Smart Core/Shell Nanorod Arrays". . . . .                                | 2  |
| Figure 2  | Schematic representation of the several steps in an ALD cycle. . . . .                                       | 5  |
| Figure 3  | Desired coverage factors in ALD. . . . .   | 6  |
| Figure 4  | Illustration of the ALD reactor with shower-head electrode. . . . .  | 7  |
| Figure 5  | Hexagonal wurtzite structure model of ZnO. . . . .   | 9  |
| Figure 6  | Schematic of the lithography process. . . . .  | 12 |
| Figure 7  | Basic scheme of electron beam lithography in combination with ALD. . . . .                                   | 13 |
| Figure 8  | Schematic of the lift off process. . . . .   | 13 |
| Figure 9  | Visualization of the experimental setup. . . . .   | 17 |
| Figure 10 | Plasma reactor used for the depositions, before and after the changes. . . . .                               | 18 |
| Figure 11 | Template for structuring the PVA. . . . .  | 23 |
| Figure 12 | Structured PVA with deposited ZnO on top. . . . .  | 24 |
| Figure 13 | Direct lithography in the reactor. . . . .   | 24 |
| Figure 14 | Basic principle of ellipsometry. . . . .   | 27 |
| Figure 15 | Model of ellipsometry data by the software CompleteEASE. . . . .   | 29 |
| Figure 16 | Setup for in situ ellipsometry measurement. . . . .  | 29 |
| Figure 17 | Measurement geometry in a XRR setup. . . . .   | 30 |
| Figure 18 | Schematic for participating wave vectors in XRR of a multilayer system. . . . .                              | 31 |
| Figure 19 | XRR schematic and XRR profile. . . . .   | 31 |
| Figure 20 | Experimental setup of the Panalytical Empyrean diffractometer. . . . .                                       | 32 |
| Figure 21 | Growth saturation curve by varying the DEZ dose. . . . .   | 35 |
| Figure 22 | $\theta/2\theta$ -scan of ZnO films deposited with different DEZ doses. . . . .                              | 36 |
| Figure 23 | Growth saturation curve by varying the O <sub>2</sub> -plasma dose. . . . .                                  | 37 |
| Figure 24 | Growth saturation curve by varying the purging time after the DEZ dose. . . . .                              | 38 |
| Figure 25 | Growth saturation curve by varying the purging time after the plasma dose. . . . .                           | 39 |
| Figure 26 | $\theta/2\theta$ -scan of ZnO films deposited with different times of purging after the plasma dose. . . . . | 39 |

|           |   |    |
|-----------|---|----|
| Figure 27 | $\theta/2\theta$ -scan of ZnO films deposited with the optimum recipe under new and old reactor conditions. . . . . | 41 |
| Figure 28 | FTIR transmittance spectrum of double-polished Si-wafers deposited with ZnO with the optimum recipe. . . . .        | 41 |
| Figure 29 | Process of lift-off with PVA. . . . .   | 44 |
| Figure 30 | Structure of ZnO after direct lithography. . . . .  | 44 |
| Figure 31 | AFM image of the EBL samples before and after the ALD process. . . . .  | 45 |
| Figure 32 | SEM images of starred pattern during the lift-off process. . . . .  | 46 |
| Figure 33 | SEM images of squared pattern during the lift-off process. . . . .  | 47 |
| Figure 34 | Schematic for the comparison of lift-off behaviour between different coatings. . . . .                              | 48 |
| Figure 35 | X-ray reflectivity profiles of ZnO grown on PMMA. . . . .   | 50 |
| Figure 36 | Three layer model from ellipsometer measurement. . . . .  | 51 |
| Figure 37 | GIXD-map of ZnO grown on a Si-substrate and ZnO grown on a polymer. . . . .   | 53 |
| Figure 38 | Temperature profile for the measurement of the glass transition temperature. . . . .                                | 54 |
| Figure 39 | Glass transition temperature $T_g$ of PMMA and PMMA+ZnO. . . . .  | 55 |
| Figure 40 | Glass transition temperature $T_g$ of PMMA and plasma treated PMMA. . . . .   | 55 |

## LIST OF TABLES

---

|          |  |    |
|----------|--|----|
| Table 1  | Physical properties of ZnO. . . . .  | 10 |
| Table 2  | Instruments for experimental setup. . . . .  | 18 |
| Table 3  | Variation of precursor dose . . . . .  | 20 |
| Table 4  | Variation of plasma dose . . . . .   | 21 |
| Table 5  | Variation of purging time after precursor dose   | 21 |
| Table 6  | Variation of purging time after plasma dose . .  | 22 |
| Table 7  | Characterization techniques. . . . .   | 28 |
| Table 8  | Optimum recipe . . . . .   | 40 |
| Table 9  | Thicknesses of layers for comparison before and<br>after lift-off . . . . .                | 48 |
| Table 10 | Reference values of PMMA and ZnO . . . . .   | 49 |
| Table 11 | Thicknesses of layers of PMMA and ZnO mea-<br>sured by spectroscopic ellipsometry. . . . . | 52 |

## ACRONYMS

---

|       |  |
|-------|--|
| AFM   | Atomic force microscopy                              |
| ALD   | Atomic layer deposition                              |
| CVD   | Chemical vapor deposition                            |
| DEZ   | Diethyl zinc ( $C_2H_5$ ) <sub>2</sub> Zn            |
| EBL   | Electron beam lithography                            |
| FTIR  | Fourier transform infrared spectroscopy              |
| GIXD  | Grazing incidence x-ray diffraction                  |
| GPC   | Growth per cycle                                     |
| PEALD | Plasma-enhanced atomic layer deposition              |
| PMMA  | Polymethyl methacrylate ( $C_5O_2H_8$ ) <sub>n</sub> |
| PVA   | Polyvinyl acetate ( $C_4H_6O_2$ ) <sub>n</sub>       |
| RF    | Radio frequency                                      |
| SE    | Spectroscopic ellipsometry                           |
| SEM   | Scanning electron microscopy                         |
| XRD   | X-ray diffraction                                    |
| XRR   | X-ray reflectivity                                   |
| ZnO   | Zinc oxide   |

## INTRODUCTION

---

The ERC-sponsored project “Smart Core” [1], conceived by my supervisor Anna Maria Coclite, aims at developing hybrid materials, which react simultaneously to multiple stimuli and therefore act as artificial skin in a broad field of application. The material will consist of a smart core that responds to temperature and humidity, while the smart shell material will sense the pressure. Any change in thickness of the smart core will be recorded by the piezoelectric shell material, which converts the signal in a measurable potential. The use of vapor-based thin film deposition techniques will allow the obtainment of this construction, consisting of nanostructured materials. The topic of my master thesis deals with the development of zinc oxide nanostructures as a shell material using a combination of Atomic Layer Deposition (ALD) and lithographic techniques.

ALD is a vapor phase thin film deposition technique, which has several advantages compared to other chemical deposition techniques. It enables the deposition of films at room temperature with a high material quality, good uniformity, precise conformality and accurate thickness control. This technique has emerged as a powerful tool in the fabrication of semiconductor devices and has been gaining a lot of recognition in research lately [2] [3].

The process of ALD relies on the alternate pulsing of precursor and reactant gases, separated by purge steps, resulting in self-limiting surface reactions. Due to the cyclic nature of the process, the material is deposited layer-by-layer and therefore guarantees a precise thickness growth control at sub-nanometer level [4]. Plasma Enhanced Atomic Layer Deposition (PEALD) is a branch of ALD, which allows due to the high reactivity of the plasma species deposition at low temperatures (room temperature) and more degrees in freedom of condition and material tuning [5].

As pressure sensing shell material, the wide-bandgap semiconductor zinc oxide (ZnO) was chosen, which is a perfect candidate because of its semiconducting and piezoelectric properties [6] [7]. Zinc Oxide (ZnO) is used in a wide field of industrial application, for example as transparent material for electrodes for solar cells. Furthermore, it is an auspicious material for lithium-ion batteries, since it is environmentally friendly and cheap. ZnO is also utilized in medicine, and products like baby powder and sun screen, as it is non-irritating and non-allergic [8].

In the wide area of lithography, shadow mask lithography and Electron Beam Lithography (EBL) were chosen to structure polymers,

which serve as a mask for the deposited ZnO.

The basic idea of the ERC project is to deposit with the help of ALD zinc oxide in a way that the Smart Material can be embedded. Then the entire construct is cut out and placed on a substrate, as shown in Figure 1.

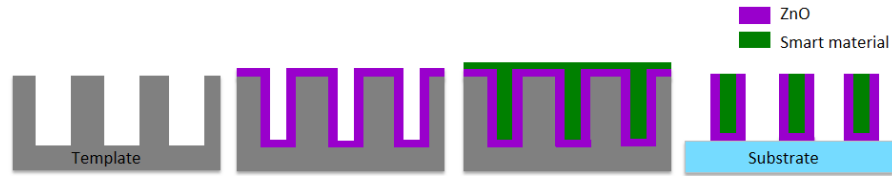


Figure 1: Schematic of the process obtaining "Smart Core/Shell Nanorod Arrays".

Summarizing all this, the aim of this work was to investigate how lithography could be integrated into the process of nanostructuring zinc oxide [9] [10]. Therefore, the first task was to optimize the exposure times for each step of the ALD cycle. Then first trials with shadow mask lithography [2] were done, followed by experiments with Electron Beam Lithography [11]. Additionally, the growth and behavior of ZnO on polymers was investigated.

## Part I

### FUNDAMENTALS

In this first part the fundamentals of plasma-enhanced atomic layer deposition and the lithographic techniques which were used are explained. Furthermore, the deposited material zinc oxide is discussed.



## ATOMIC LAYER DEPOSITION

Plasma Enhanced Atomic Layer Deposition (PEALD) is a vapor phase thin film deposition technique, where reactive species are created in a plasma phase at room temperature. This chapter describes the process of ALD with the help of the books "Atomic Layer Deposition" by Tommi Kääriäinen, David Cameron, Marja-Leena Kääriäinen and Arthur Sherman [12], "Atomic Layer Deposition of Nanostructured Materials" edited by Nicola Pinna and Mato Knez [5] and the book chapter "Atomic Layer Deposition" by Harm Knoop et al [13]. ALD relies on successive, surface-controlled reactions from the gas phase in order to create thin films in the nanometer range by the alternate pulsing of precursor and reactant gases, which are separated by purging steps [14]. The principle of ALD is schematically visualized in Figure 2.

A typical ALD cycle consists of four steps:

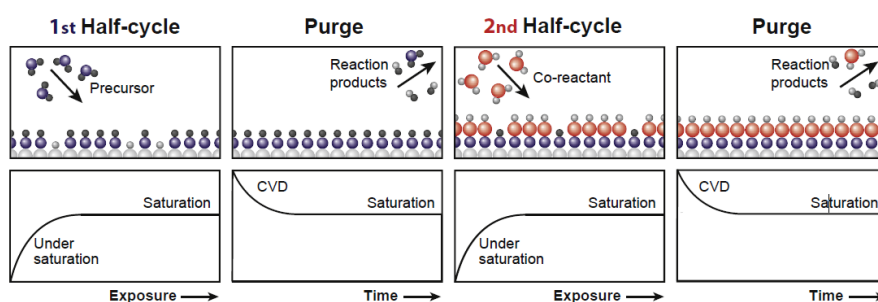


Figure 2: Schematic representation of the several steps in an ALD cycle. In the lower panels the resulting coverage, or Growth Per Cycle (GPC) as a function of time is shown. For insufficient exposure times incomplete saturation and therefore a CVD-like growth is obtained. Image reprinted from [13]

1. *Precursor step*: The precursor, typically a metal center surrounded by chemical functional groups, is pulsed into the reactor and adsorbs to the active sites on the substrate.
2. *Postprecursor Purge*: An inert gas is flown into the chamber, in order to remove any excess precursor molecules. This is necessary to avoid reactions between precursor and co-reactant molecules directly in the gas phase or on the surface, as this could lead to an undesired CVD component.

3. *Co-reactant step*: The co-reactant, which is usually a non-metal, is pulsed into the reactor and reacts with the surface species in order to obtain the desired film composition.
4. *Postreactant Purge*: The same applies as for step 2.

The reactants in the first half-cycle (precursor) and second half-cycle (co-reactant) are self-limiting, which means the process stops when all available surface sites have reacted. The steps mentioned above, give one reaction cycle. During each reaction cycle a fixed amount of material is deposited, this amount is known as Growth Per Cycle (GPC), which is ideally one monolayer of deposited material. The GPC as a function of exposure time, as shown in Figure 2, gives the so called saturation curves. For long enough exposure times saturated growth is obtained, while too short dosing times could lead to a CVD-like growth, where the precursors react at the same time on the surface [3].

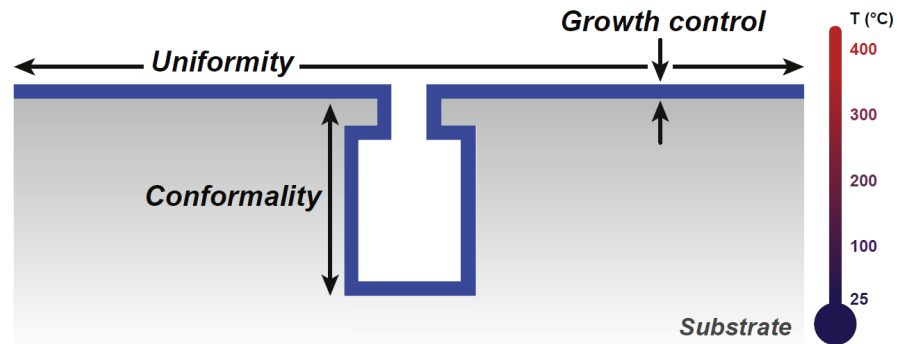


Figure 3: Desired coverage factors in ALD. Image reprinted from [13]

With ALD, growth control is obtained in several ways (see Figure 3). Due to the layer-by-layer deposition of high-quality thin films, thickness control at subnanometer level is assured. Furthermore, the uniformity and conformality for surface features, including pores, trenches and surface roughness is excellent. And even at low temperatures PEALD enables the deposition of high purity and high density materials.

## 2.1 PLASMA ENHANCED ATOMIC LAYER DEPOSITION

PEALD is a variant of ALD, that offers certain benefits compared to thermal ALD. The high reactivity of the plasma species allows depositions at lower temperatures and more degrees in freedom of condition and material tuning.

A plasma is a state of matter in which free, charged particles among other gas phase species become highly conductive. Plasma is so

called quasi neutral, that means that the electron density is over a large volume approximately the same as the ion density. Generally, a plasma is generated through acceleration and heating electrons of a neutral gas, done by an electrical field. These energized electrons ionize gas-phase species and newly charged particles are created when these charge carriers collide with atoms or molecules. This results in an avalanche of charged particles, which is balanced by charge carrier losses, so that a steady-state plasma develops. A plasma provides a high, diverse but selective reactivity without heat to a surface since in cold plasmas only the electrons are heated.

PEALD has several merits towards thermal ALD [5]:

- *Improved material properties:* Due to the high reactivity of the plasma, properties like the film density, the impurity content and the electronic properties are enhanced.
- *Deposition at reduced substrate temperatures:* The reactive species are created because of the plasma, therefore less thermal energy is required for the ALD process.
- *Good control of film composition:* With the settings of the plasma (operating pressure, plasma power, plasma exposure time) it is easier to control the surface chemistry.
- *Increased growth rate:* Because of the high reactivity of the plasma, a higher density of reactive species is created, which leads to a higher growth per cycle (GPC).

In our lab we use a showerhead electrode, illustrated in Figure 4. With a radio frequency (RF) of 13.56 MHz between two parallel electrodes a plasma is generated. The top electrode is powered, while the other one is grounded. The substrate is placed on the grounded electrode and the gases are brought into the reactor via a showerhead. Since the substrates are directly positioned at the ground electrode, this set-up of ALD is accounted to "direct plasma ALD".

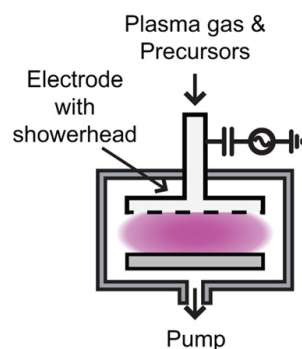


Figure 4: Illustration of the ALD reactor with showerhead electrode. Image reprinted from [5].



## BASIC PROPERTIES OF ZINC OXIDE

This chapter brings out the general properties of zinc oxide (ZnO). More detailed information can be found in the book "Zinc oxide: Fundamentals, Materials and Device Technology." by Hadis Morkoç and Ümit Özgür. [7]. The most important physical properties of ZnO are listed in Table 1.

Zinc oxide is a wide band gap semiconductor of the type II-VI with a band gap of  $E_g = 3.437$  eV at 4 K and a hexagonal wurtzite crystal structure (see Figure 5) [6]. This wurtzite structure consists of a

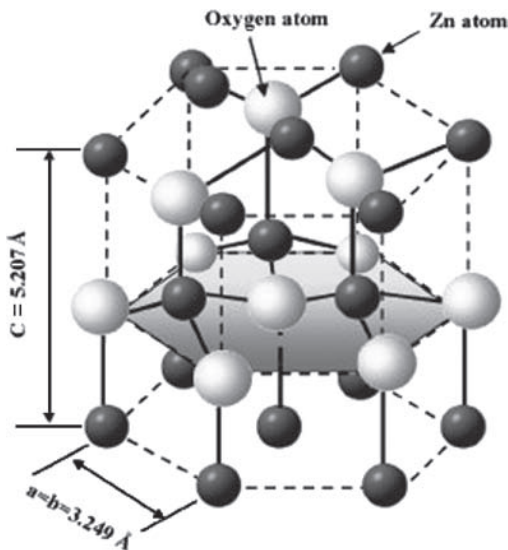


Figure 5: Hexagonal wurtzite structure model of ZnO. Image reprinted from [8]

hexagonal unit cell with two lattice parameters  $a = 3.25$  Å and  $c = 5.2$  Å. Their ratio is approximately  $\frac{c}{a} = 1.60$ . It belongs to the space group of  $C_{6V}^4$  in the Schoenflies notation or  $P6_3mc$  in the Hermann-Mauguin notation.

Figure 5 visualises the structure, which consists of two inter-penetrating hexagonal closed pack (hcp) sublattices, where each has one type of atom, Zn or O. As typical for the II-VI semiconductors, the bonding happens widely via ionic bondings ( $Zn^{2+} - O^{2-}$ ) with a radius of 0.074 nm for  $Zn^{2+}$  and 0.140 for  $O^{2-}$ . This fact contributes to the strong piezoelectricity of ZnO.

ZnO is significantly softer than other relevant semiconductors, such as GaN. It has a Mohs Hardness of 4. The melting point lies at 1975 °C and the density is 5.606 g/cm<sup>3</sup>. Compared to other tetrahedrally

Table 1: Physical properties of ZnO [8].

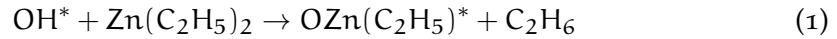
| PROPERTIES                   | ZNO  |
|------------------------------|--|
| Lattice parameters at 300 K  |  |
| - $a_0$                      | 0.032495 nm  |
| - $c_0$                      | 0.52069 nm   |
| - $\frac{c_0}{a_0}$          | 1.602  |
| Density                      | 5.606 g/cm <sup>3</sup>  |
| Stable phase at 300 K        | Wurtzite   |
| Melting point                | 1975 °C  |
| Thermal conductivity         | 0.6  |
| Linear expansion coefficient | $a_0$ : 6.5 cm <sup>3</sup> x 10 <sup>-6</sup><br>$c_0$ : 3.0 cm <sup>3</sup> x 10 <sup>-6</sup> |
| Static dielectric constant   | 8.656  |
| Refractive index             | 2.008  |
| Band gap (4 K)               | 3.437 eV   |

bonded semiconductors, ZnO is the one with the highest piezoelectric tensor, which makes it very interesting for many applications.

### 3.1 APPLICATION OF ZNO IN ATOMIC LAYER DEPOSITION

There are various combinations of precursors along with co-reactants, substrate materials and deposition temperatures. In our set-up the following materials are used:

For the deposition of ZnO the most common *precursor* diethyl zinc (DEZ) is used. DEZ is a highly pyrophoric organozinc compound consisting of a zinc center bound by two ethyl groups and has the chemical formula C<sub>4</sub>H<sub>10</sub>Zn. The two chemical ALD half-reactions can be written as:



where \* marks a surface species.

The *co-reactant* is represented by oxygen plasma, which allows the growth of films with a higher degree of stoichiometry at room temperature.

The *purging* happens with argon.

## LITHOGRAPHY

---

In this chapter the two lithographic techniques, which were used for the experiments in this thesis, are described.

### 4.1 SHADOW MASK LITHOGRAPHY

#### 4.1.1 *Polyvinyl alcohol*

Polyvinyl alcohol (PVA) is a water-soluble linear polymer with the idealized formula  $[\text{CH}_2\text{CH}(\text{OH})]_n$ . Beside its applications in paper making and textiles, it is also used for a wide range of coatings. Its UV transparency, mechanical strength, as well as the thermal durability of PVA are good enough for usage in lithography.

#### 4.1.2 *Operating Principle*

The method that is used here is a variation of shadow mask lithography. It meets the demands of being easy to perform and there is no need for any high tech devices. The basic idea is to have a template, that is fixed onto a substrate. This substrate is then spincoated with a polymer. Afterwards the template is removed and one obtains the polymer mask for the metal compound deposition. The final step is the lift-off step, where the polymer and the excess material on top of it is removed and the desired metal compound structure remains.

The idea to realize lithography with the water soluble PVA is not new and was often tried with different lithographic techniques and different deposition techniques [4]. The process of nanoimprinting lithography works very well with a PVA mask and structures in the nanometer range could be achieved [9].

### 4.2 ELECTRON BEAM LITHOGRAPHY

#### 4.2.1 *Polymethyl methacrylate*

Polymethyl methacrylate (PMMA) is a polymer (also called acrylic glass) and has the chemical formula  $(\text{C}_5\text{O}_2\text{H}_8)_n$ . Due to its excellent resistance against UV-light and weathering, it is the resist of choice for electron beam lithography.

The glass transition temperature  $T_g$  of atactic PMMA lies at 125°C. Since commercial PMMA is often co-polymerized with co-monomers that differ from methyl methacrylate, the  $T_g$  is not a certain value, but

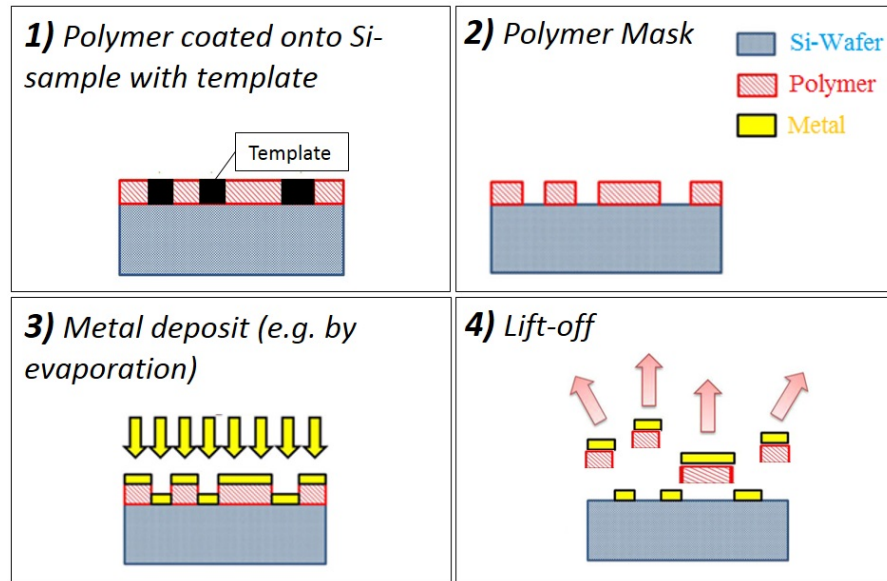


Figure 6: Schematic of the lithography process.

a temperature range from approximately 87 to 157°C. [15]

#### 4.2.2 Operating principle

Electron Beam Lithography (EBL) is a technique, where an accelerated beam of electrons is used to draw patterns in nanometer range on a substrate. These substrates are coated with an electron sensitive resist, that changes its solubility when it is exposed to high-energy electrons.[11] Here PMMA is used, which is a positive resist. That means that the exposed area is more soluble and therefore dissolves in a suitable dissolver like acetone. The benefit of this technique is the possibility to draw customized patterns without a mask in a high resolution in the nanometer range. The resulting pattern then acts as a mask for the ALD deposition. In the end, a final lift-off step removes the resist mask and the excess material in top of it and the requested structured ZnO should remain on the substrate surface. The individual steps can be seen in Figure 7.

#### 4.3 QUESTION OF LIFT-OFF

Biercuk et al. [10] did the structuring by photolithography using the Shipley photo-resist and by EBL. Then  $\text{HfO}_2$  and  $\text{Al}_2\text{O}_3$  were deposited by ALD at temperatures between 100-150 °C. The lift-off was performed by putting the samples in acetone and structures in the range of 2.5–100 nm and sub-micron lateral resolution were obtained.

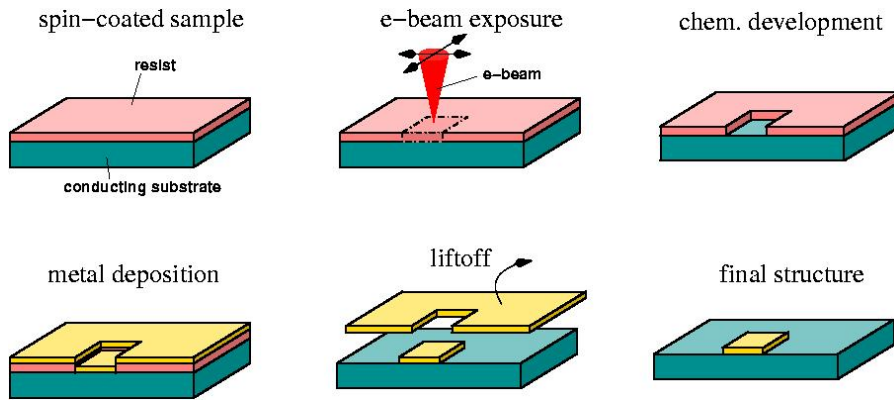


Figure 7: Basic scheme of electron beam lithography in combination with ALD. Image reprinted from [16].

Another approach was done by Suresh et al. [4] using nanoimprint lithography (NIL). In this case periodic patterned molds were used to create nanoporous PMMA. Then, zinc oxide was deposited by ALD at a temperature of 70 °C. The lift-off in acetone put forth a periodic array of ZnO structures.

The main question is how the lift-off will work. For unconformal deposition techniques this works well, but we don't know where the conformal zinc oxide film will be attacked. It is possible that the film will break at the side walls, or that the side walls will even remain, as shown in Figure 8.

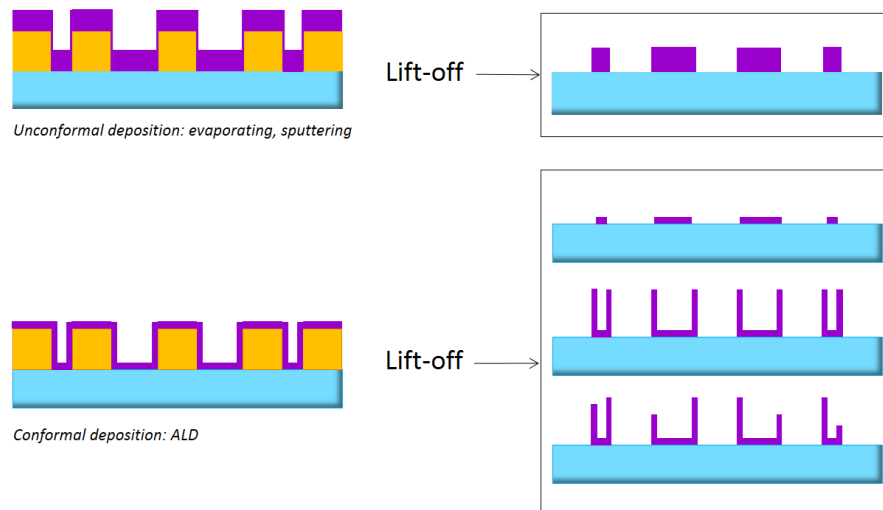


Figure 8: Schematic of the lift off process. Top: Lift-off for unconformal deposition techniques, bottom: lift-off for conformal deposition techniques.



## Part II

### EXPERIMENTAL

This part consists of the description of the optimization for the deposition recipe and the experiments with lithographic techniques. Furthermore, the utilized analyzing methods are discussed.



## SETUP AND RECIPE OPTIMIZATION

### 5.1 SETUP

In Figure 9 the schematic experimental setup is shown. The used devices are listed in Table 2.

The function of each device and the exact procedure is described in the master thesis of Julian Pilz [17], who worked with this setup before me. The reactor is a custom-built direct plasma reactor and can

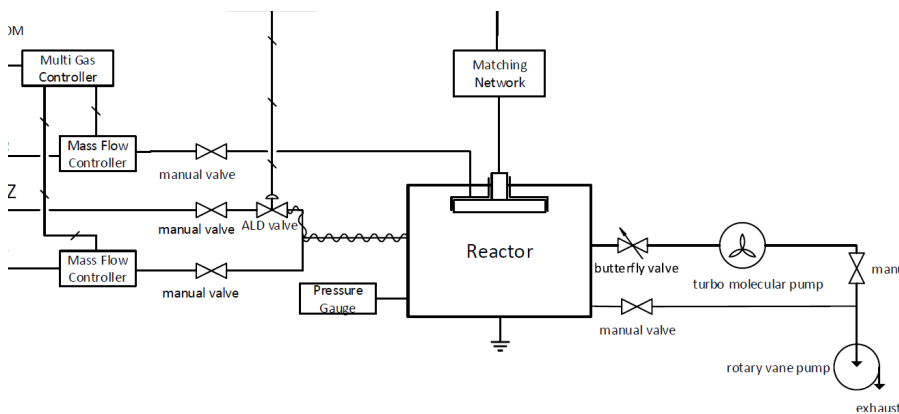


Figure 9: Visualization of the experimental setup. Crossed lines correspond to signal transmission line, sinusoidal line corresponds to heated line. [17]

be seen in Figure 10. The shower head radio frequency (RF) electrode and the ground electrode are 20 and 30 cm in diameter. In order to obtain milder and better distributed plasma conditions, the reactor was extended in height, so that the top-electrode grid (shower head) is more distanced from the substrates than before (see Figure 10). As a result, the volume of the reactor increased and the clearance between the shower head RF electrode and the ground electrode was enlarged from 4 cm to 8 cm. This is the reason why the ALD process was optimized again.

Table 2: Instruments for experimental setup.

| DEVICE                | MODEL                            |
|-----------------------|----------------------------------|
| Arduino               | Arduino Uno                      |
| Relais module         |                                  |
| RF power generator    | Advanced Energy Cesar 13.560 MHz |
| Matching network      | Advanced Energy Navio            |
| Multi gas controller  | MKS 647C                         |
| ALD valve             | Swagelok ALD 3                   |
| Mass flow controller  | MKS MF1-C                        |
| Butterfly valve       |                                  |
| Turbo molecular valve | Pfeiffer Vacuum TMH071P          |
| Rotary vane pump      | Pfeiffer Vacuum DUO5M            |
| Pressure gauge        |                                  |

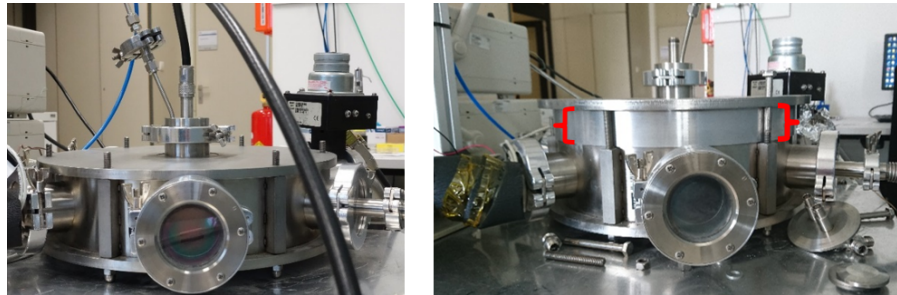


Figure 10: Plasma reactor used for the depositions. Left: Plasma reactor before the changes. Precursor and argon are flown in from the left, oxygen from the top. The black coaxial is the connection between the RF-electrode and the matching network. Right: Plasma reactor after changing. Clearance between top and ground electrode is enlarged.

## 5.2 RECIPE OPTIMIZATION

In order to optimize the process of plasma enhanced atomic layer deposition, it is important to minimize the duration of each of the four steps, which are explained in Chapter 2. Therefore several series of depositions with different parameters are performed.

1. Precursor dose
2. Purging after precursor dose
3. Plasma dose
4. Purging after plasma dose
5. Number of Cycles

For all depositions described in this thesis the plasma power is constantly used at 60 W.

For each of the optimization series there are always 100 ALD cycles performed.

Since the self limiting ALD surface reactions build upon the density and allocation of surface reaction sites and precursor properties, the Growth per Cycle, which is ideally one monolayer of deposited material, is expected to be comparable with further results [17], regardless of the ALD reactor setup [18].

For an appropriately designed ALD process, every step has to be saturated. This means that the precursor dose has to be long enough to suffuse the entire substrate with precursor molecules, the exposure of plasma has to be long enough for a full oxidisation of the surface and the purging times have to be long enough to remove all excess precursor molecules and oxidising species from the reactor to avoid a CVD-like growth behavior.

### 5.2.1 Procedure

As substrates, polished Silicon(100) wafers with a native oxide are used. With a diamond tip they are diced into squares with an approximate side length of 2 cm. The substrates are then cleaned with isopropyl alcohol and compressed CO<sub>2</sub> flow. For each deposition at least four substrates are evenly distributed in the reactor to ensure the homogeneous growth of zinc oxide.

After the lid closes the reactor, the valve to the rotary vane pump is opened. One minute later one can open the connection to the pressure gauge. When a pressure below 150 mTorr is reached, the butterfly valve is opened and the turbo molecular pump is turned on. The valve from the rotary vane pump is closed and the valve to the turbo molecular pump is opened. Now the turbo molecular pump brings

the pressure in the reactor down to a base pressure, where the leak rate should be below a value of approximately 0.08 sccm. Then the butterfly valve is put at a fixed opening of 35 % for the purpose of having a pressure of around 130 mTorr during the plasma exposure. The line connection between the DEZ and the reactor is heated with heating wires to 40°C. The valves to the DEZ, oxygen and argon are opened and the power generator is turned on. The setting of the matching network is switched to the automatic mode. The Arduino and multi gas controller are connected to the PC. The flow rates for oxygen and argon are set to 20 sccm at the multi gas controller for all depositions. The requested deposition parameters are entered into the Labview program and the deposition is started.

### 5.2.2 Variation of precursor dose

In this set of depositions the precursor dose is varied, while the other values are held at times where they are expected to be in saturation [17]. The parameters for this depositions are listed in Table 3.

Table 3: Variation of precursor dose

| DEZ DOSE / S | PURGE / S | PLASMA DOSE / S | PURGE / S |
|--------------|-----------|-----------------|-----------|
| 0.005        | 20        | 10              | 30        |
| 0.010        | 20        | 10              | 30        |
| 0.015        | 20        | 10              | 30        |
| 0.020        | 20        | 10              | 30        |

### 5.2.3 Variation of plasma dose

In this set of depositions the plasma dose is varied, while the other values are held at times where they are in saturation. The parameters can be seen in Table 4.

### 5.2.4 Variation of purging time after precursor dose

In this set, the purging time after the DEZ dose is varied, while the other parameters are held at values where saturated growth is ensured. The deposition parameters are listed in Table 5.

Table 4: Variation of plasma dose

| DEZ DOSE / S | PURGE / S | PLASMA DOSE / S | PURGE / S |
|--------------|-----------|-----------------|-----------|
| 0.015        | 20        | 1               | 30        |
| 0.015        | 20        | 3               | 30        |
| 0.015        | 20        | 5               | 30        |
| 0.015        | 20        | 6               | 30        |
| 0.015        | 20        | 7               | 30        |
| 0.015        | 20        | 8               | 30        |
| 0.015        | 20        | 9               | 30        |
| 0.015        | 20        | 10              | 30        |

Table 5: Variation of purging time after precursor dose

| DEZ DOSE / S | PURGE / S | PLASMA DOSE / S | PURGE / S |
|--------------|-----------|-----------------|-----------|
| 0.015        | 16        | 8               | 30        |
| 0.015        | 10        | 8               | 30        |
| 0.015        | 8         | 8               | 30        |
| 0.015        | 5         | 8               | 30        |
| 0.015        | 4         | 8               | 30        |

### 5.2.5 Variation of purging time after plasma dose

In this set, the purging time after the plasma dose is varied, while the other parameters are held at values where saturated growth is ensured. The deposition parameters are shown in Table 6.

### 5.2.6 FTIR measurement

In order to investigate the contaminations of Carbon in the ZnO film, deposited with the new optimum recipe, a FTIR measurement is performed. The used device is a BOMEM FT-IR Spectrometer MB102. Therefore, double-polished Si-wafers with an (100) orientation and a thickness of 525  $\mu\text{m}$ , are cut into an approximate size of 2 cm x 2 cm and cleaned with isopropyl alcohol and compressed CO<sub>2</sub> flow. With the same procedure as described in section 5.2.1, the substrates are brought into the reactor and deposited with ZnO. The deposition parameters are listed in Table 8.

Before and after the FTIR measurement of the deposited double-polished Si-wafers, a pristine substrate is measured as a reference spectrum. The received spectrum of the ZnO films is then divided by this reference spectrum. The obtained resolution of this measurement is 4

$\text{cm}^{-1}$  and the measurement environment is purged with  $\text{CO}_2$ .

Table 6: Variation of purging time after plasma dose

| DEZ DOSE / S | PURGE / S | PLASMA DOSE / S | PURGE / S |
|--------------|-----------|-----------------|-----------|
| 0.015        | 12        | 8               | 30        |
| 0.015        | 12        | 8               | 25        |
| 0.015        | 12        | 8               | 22        |
| 0.015        | 12        | 8               | 20        |
| 0.015        | 12        | 8               | 16        |
| 0.015        | 12        | 8               | 12        |

## SHADOW MASK LITHOGRAPHY

---

### 6.0.1 *Spincoating*

In order to obtain structures on the Si-wafers, which should serve as a mask during the ALD, a Si-wafer is cut into the size of 2 cm x 2 cm and afterwards is cleaned. Before the substrate is spincoated, a template is fixed on it (see Figure 11).

Then the substrate is spincoated with PVA. For the PVA solution, 20,2 mg PVA particles are diluted in 2 ml distilled water, and heated up to 50 °C. After spincoating, the sample is put on the heating plate for 5 min at 50 °C. Afterwards the mask is removed and structured PVA is left on the Si-wafer.



Figure 11: Template for structuring the PVA.

### 6.1 ATOMIC LAYER DEPOSITION

The PVA now represents a mask for the ALD process. The prepared substrate is then deposited by ALD. The parameters for this deposition are shown in Table 8, where 250 cycles are deposited. In Figure 12 the sample with PVA and ZnO on top can be seen.

### 6.2 LIFT OFF

The lift-off for the sample happens for the first 20 min in deionized water and then another 20 min in an ultra-sonic bath. The progress is checked with the optical microscope.

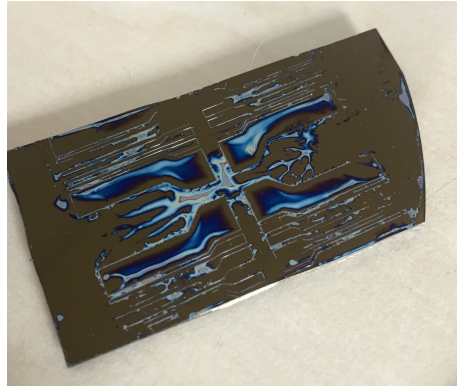


Figure 12: Structured PVA with deposited ZnO on top.

### 6.3 DIRECT LITHOGRAPHY

It is tested by putting a template directly on a substrate in the reactor during deposition.

For this, the mask, which was used for former experiments, is put on a diced and cleaned substrate and weighted with ceramics (see Figure 13). Under optimum conditions 200 cycles are deposited. After the deposition, the sample is measured by SE and analyzed for conformality.



Figure 13: Direct lithography in the reactor. Mask is weighted with ceramics during the deposition.

## ELECTRON BEAM LITHOGRAPHY

---

The following steps were performed at the Karl Franzens University Graz with the help of Prof. Joachim Krenn and Prof. Andreas Hohenau.

### 7.1 SPINCOATING

The first step is to spincoat well prepared (cut and cleaned) Si-wafers with the resist PMMA, diluted with Ethyl lactate in a ratio of 2:1. Subsequently the samples are put on a heating plate to dry.

### 7.2 ELECTRON BEAM LITHOGRAPHY

For the EBL process a RAITH 100-2 turnkey system based on a ZEISS Gemini field emission SEM and a JEOL 6400 tungsten cathode SEM equipped with a RAITH Quantum lithography unit is used.

For loading the samples into the gadget, the samples, which should be patterned, are firmly mounted on the sample holder. Then the airlock is closed and the system is evacuated.

After aligning the sample, the parameters for the EBL process are set. In a total area of  $1300 \times 100 \mu\text{m}$  a patterning raster of 2.5 nm and an area step size of 5 nm are set. For the form of the pattern, squares in two different sizes and stars are chosen.

Then the samples are unloaded and put for 30 s into a developer (isopropanol) and for another 30 s into a stopper (deionized water).

### 7.3 ATOMIC LAYER DEPOSITION

For later reference measurements about the thickness change and the growth of ZnO on polymer, the thickness of the PMMA is measured by ellipsometry. For these measurements unpatterned samples are used.

Also AFM imaging is used to check the structure of the patterns before and after the deposition of ZnO (see Figure 31).

The structured PMMA serves as a mask for the ALD process. The prepared EBL samples, plus the unpatterned PMMA samples are deposited by ALD under the conditions of the optimum recipe (see Table 8).

#### 7.4 LIFT-OFF

To remove the PMMA and the excess material on top of it, a lift-off is performed. For the lift-off step the samples are put into a beaker, filled with acetone. This beaker is put into an ultra sonic bath for a total duration of 180 min. After every 30 min the progress is checked with the SEM.

## CHARACTERISATION TECHNIQUES

This chapter explains the most important characterization techniques, which are used to investigate the thin film properties like thickness, optical constants, crystallinity and the chemical composition. There are also techniques used for imaging and investigating the structure of the zinc oxide. All methods are listed in Table 7.

### 8.1 SPECTROSCOPIC ELLIPSOMETRY (SE)

The most used technique is spectroscopic ellipsometry, which enables the determination of the layer thickness and the refractive index of the deposited thin films.

In our lab we work with the J.A. Woollam Co M-2000V ellipsometer, which has a wavelength range of the incident light of 371 nm - 1000 nm. The reflected spectrum is measured for several angles, which can be preset.

The basic principle can be seen in Figure 14. Unpolarized light is sent

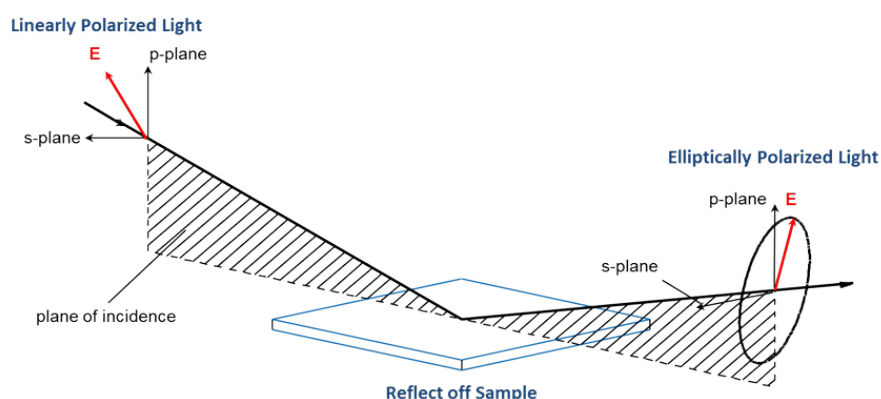


Figure 14: Basic principle of ellipsometry. Image reprinted from [19].

through a polarizer and further onto the sample surface. After interaction with the sample, the reflected beam gets elliptically polarized, depending on the thin film properties. Then, the detector converts the light into an electronic signal in order to determine the reflected polarization. This polarization change is represented as an amplitude ratio  $\Psi$  and the phase difference  $\Delta$ :

$$\frac{r_p}{r_s} = \rho = \tan \Psi \cdot e^{i\Delta} \quad (3)$$

Table 7: Characterization techniques.

| METHOD   | PROPERTIES                        |
|--|-----------------------------------|
| <i>Spectroscopic ellipsometry</i>              | Layer thickness, refractive index |
| <i>X-ray diffraction</i>                       | Crystal structure                 |
| <i>X-ray reflectivity</i>                      | Layer structure, layer thickness  |
| <i>Fourier transform infrared spectroscopy</i> | chemical composition              |
| <i>Optical Microscopy</i>                      |                                   |
| <i>Atomic Force Microscopy</i>                 | Imaging                           |
| <i>Scanning Electron Microscopy</i>            |                                   |

The collected data is processed by the software CompleteEASE [20] and for transparent materials fitted with a Cauchy Model:

$$n(\lambda) = A + \frac{B}{\lambda^2} + \frac{C}{\lambda^4} \quad , \quad (4)$$

with  $n$  the wavelength dependent refractive index,  $\lambda$  the wavelength and  $A$ ,  $B$  and  $C$  the fitting parameters. The model calculates the predicted response with the help of the Fresnel equations, in order to describe the thickness and the optical constants of the material. If these values are unknown, they are estimated and then compared to the experimental data. An estimator, like the Mean Squared Error (MSE) is used to quantify the difference between curves. Figure 15 shows the overlapping of the model and the experimental data with a very small MSE. The error for all measurements in this thesis lies in the subnanometer range. The Cauchy model is limited by the Kramers-Kronig consistency and can cause unphysical dispersion. Absorbing materials can often have a transparent wavelength region, which can be modelled with the Cauchy model. However, to cover the whole range, an oscillator model, like the Lorentz oscillator, can be used [20]:

$$\tilde{\epsilon} = \epsilon_{1 \text{ offset}} + \frac{AE_c}{E_c^2 - E^2 - iBE} \quad , \quad (5)$$

where  $A$  is the amplitude,  $B$  the broadening,  $E_c$  the center energy and  $\epsilon_{1 \text{ offset}}$  the offset. The energy  $E$  is related to the frequency of a wave:

$$E = h\nu \cong \frac{1240}{\lambda_{nm}} \quad , \quad (6)$$

where  $h$  is the Planck's constant and  $\lambda$  the wavelength.

For in situ measurements instead of the usual sample stage, a heating stage is used (see Figure 16), which allows the monitoring the

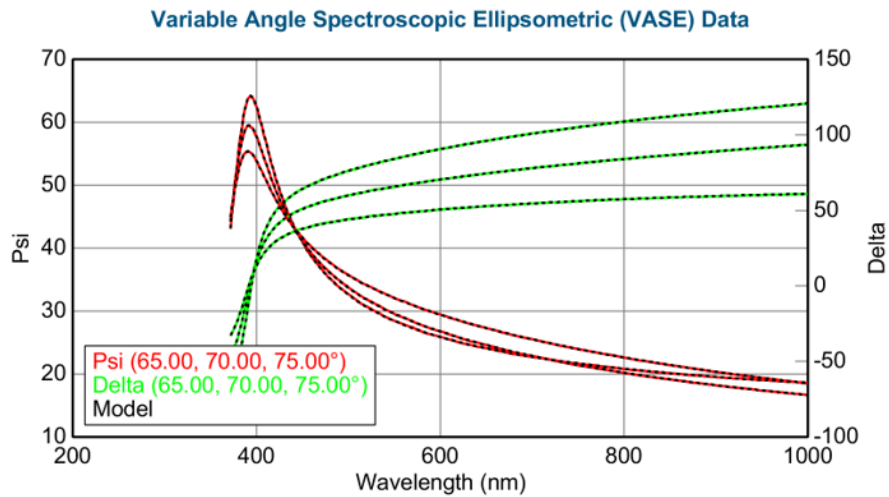


Figure 15: Model of ellipsometry data by the software CompleteEASE. Calculated and measured data overlap with a very small Mean Squared Error.

thickness change of thin films as a function of the temperature. The cooling works with the help of liquid nitrogen.

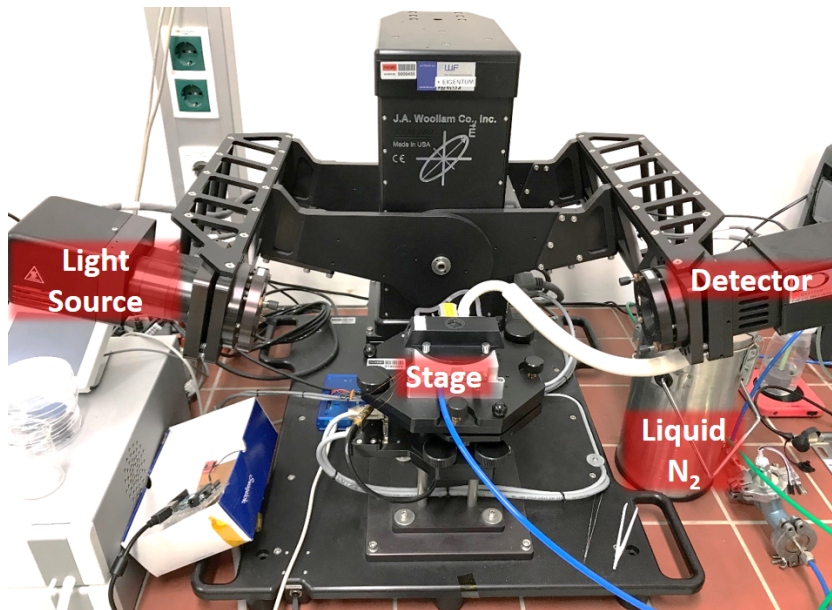


Figure 16: Setup for in situ ellipsometry measurement.

## 8.2 X-RAY REFLECTIVITY

This section should give a short overview over the method of X-ray reflectivity (XRR), since it gave important conclusions for this thesis. XRR is a surface sensitive analysis method and is used to analyse the layer thickness of thin films and multilayers, surface and interface

roughness as well as the layer density. The basic idea of this technique is measuring the reflected X-ray intensity in specular direction as a function of the incidence angle over a range of angles, which are close to the critical angle for total reflection. Figure 17 shows the XRR setup.

The calculations for multilayers are based on the Parrat formalism.

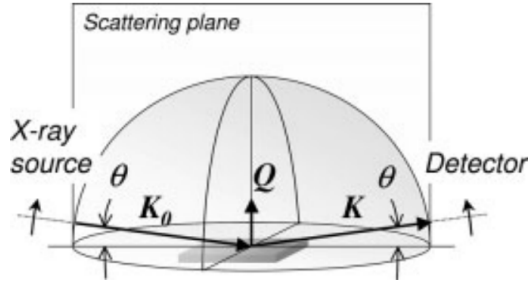


Figure 17: Measurement geometry in a XRR setup. Image reprinted from [21].

For a system of multilayers, like in Figure 18, the reflectivity is described by reflectivity coefficients  $r_{j,j+1}$  [21]:

$$r_{j,j+1} = \frac{k_{z,j} - k_{z,j+1}}{k_{z,j} + k_{z,j+1}} \quad (7)$$

where  $k_{z,j}$  and  $k_{z,j+1}$  are the  $z$  wave vector components in the two neighboring layers. For each interface  $j,j+1$  and for each layer  $j$ , a set of  $2 \times 2$  matrices is introduced. These are called in each case the refraction and the translation matrices  $R_{j,j+1}$  and  $T_j$ . The product of all of these matrices delivers the transfer matrix  $M$ , where the ratio of  $M_{12}$  and  $M_{22}$  gives the amplitude of the multilayer reflectivity.

If this procedure is applied for a single-layer system, an expression for the intensity of the reflected beam is given by:

$$\frac{I_R}{I_0} = \frac{r_{0,1}^2 + r_{1,2}^2 + 2r_{0,1}r_{1,2}\cos 2k_{z,1}t}{1 + r_{0,1}^2 r_{1,2}^2 + 2r_{0,1}r_{1,2}\cos 2k_{z,1}t} \quad (8)$$

This ratio depends on the reflection coefficients of the air-film interface (0,1) and the film-substrate interface (1,2), in accordance with Equation 7. The ratio also contributes to the oscillation phenomena, the so-called Kiessig fringes. The Kiessig fringes result from the constructive and destructive interference of reflected x-rays from two interfaces. The phase difference  $\Delta$  between two beams is given through equation 9, where  $n$  is the refractive index of the layer (see Figure 19a). With their period the layer thickness can be determined:

$$\Delta = (AB + BC)n - AD \quad , \quad (9)$$

In Figure 19b a typical XRR profile is shown. The sharp decrease is the critical angle, which depends on the material. The oscillations

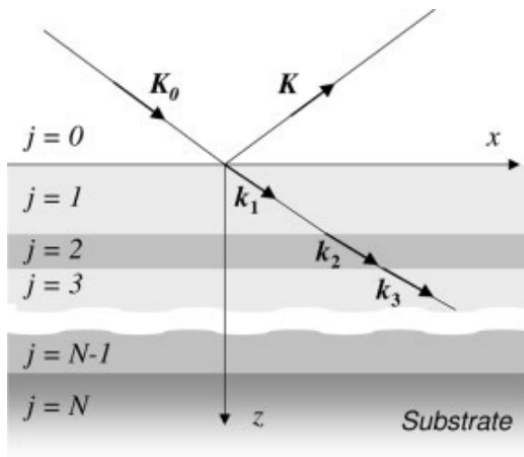
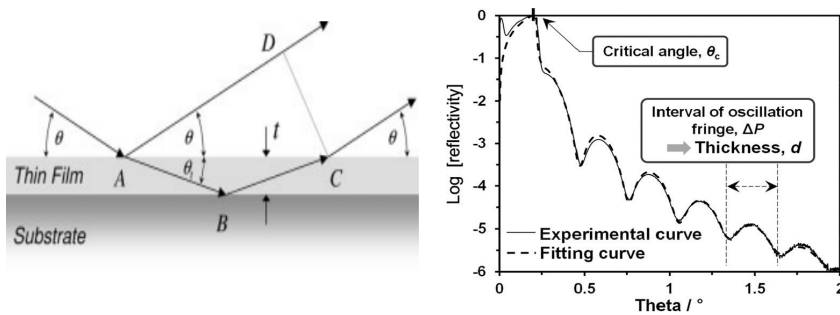


Figure 18: Schematic for participating wave vectors in XRR of a multilayer system. Image reprinted from [21].



(a) Schematic representation of reflected and refracted beams for the derivation of their phase difference  $\Delta$ . Image reprinted from [21].  
 (b) XRR profile with Kiessig fringes. Image reprinted from [22].

Figure 19: XRR schematic and XRR profile showing the Kiessig fringes.

afterwards are the Kiessig fringes. The XRR measurement is performed on a Panalytical Empyrean diffractometer, the setup can be seen in Figure 20. A  $\frac{1}{32}^\circ$ -divergence slit, a 10 mm-mask and a 0.1 mm anti-scatter slit are used for the measurement.

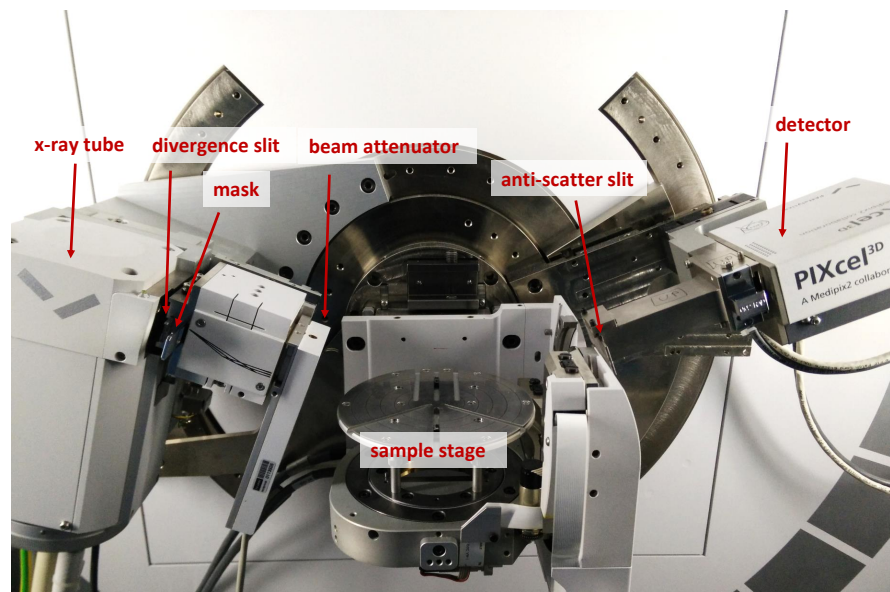


Figure 20: Experimental setup of the Panalytical Empyrean diffractometer [17].

## Part III

### RESULTS AND DISCUSSION

In this part the optimized parameters for the ALD process are presented. This part also covers the results of the trials with shadow mask lithography and the outcome of the Electron Beam Lithography experiments. Furthermore, conclusions are drawn about how ZnO grows on polymer and how the reactor conditions influence the polymer.



## DETERMINATION OF THE OPTIMUM RECIPE

In this chapter the analysis of the optimization process for the atomic layer deposition is discussed. Therefore, the growth per cycle (GPC) is used, which is ideally one monolayer of deposited material and an important parameter of ALD technique. The GPC is obtained by measuring the thickness of the thin films by spectroscopic ellipsometry, divided by the number of cycles. Compared to the term 'rate of deposition', which is used for other thin film deposition techniques, the GPC generally results in a low value [23]. The growth per cycle as a function of four ALD parameters gives the saturation curves.

## 9.1 PRECURSOR DOSE

In Figure 21 the growth per cycle depending on the DEZ dose is shown. The deposition parameters can be seen in Table 3. The GPC with respect to the precursor dose saturates quite fast and stays within the measured DEZ exposure times within a certain range of GPC. To ensure that enough precursor molecules are pulsed into the reactor for adsorbing to the active sites of the substrate, a precursor dose of 0.015 s is chosen.

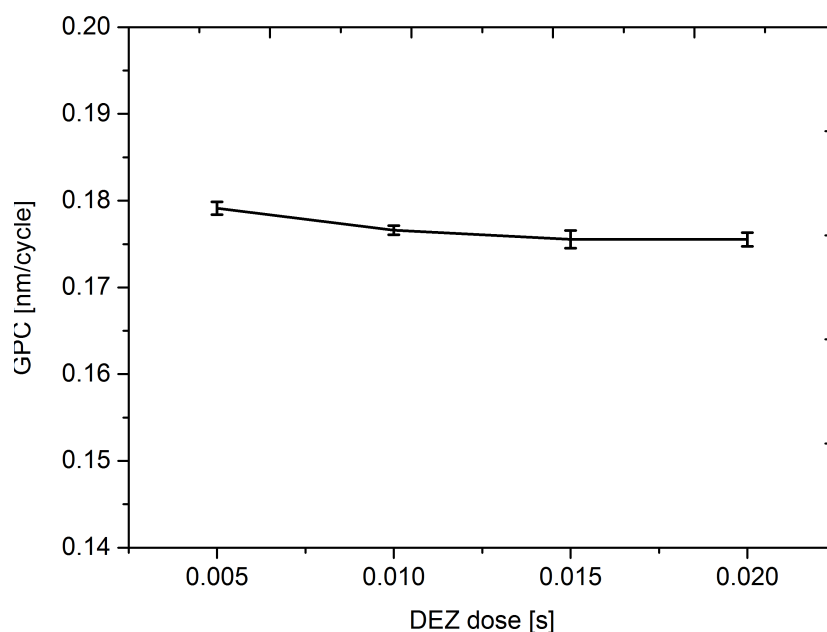


Figure 21: Growth saturation curve by varying the DEZ dose. The line serves as guide to the eye.

### 9.1.1 XRD measurements

In Figure 22 the  $\theta/2\theta$ -scan of ZnO films deposited with different DEZ doses can be seen. All samples match the (100) and the (101) peak of the ZnO reference measurement, whereby a preferential orientation in the (100) direction can be determined. The absence of the (002) peak could be attributed to an overlap with the Si (200) peak. The peak close to the (110) peak of ZnO does not belong to the zinc oxide film, since its shape is more incisive than the other ones originating from the ZnO. This peak was also noticed in XRD measurements with organic films, so it is conceivable that this peak stems from the background of the measurement table [17]. This applies for all following XRD measurements. Considering the crystalline properties of the ZnO films, which were treated in the thesis of Julian Pilz, the XRD measurements are consistent with his results.

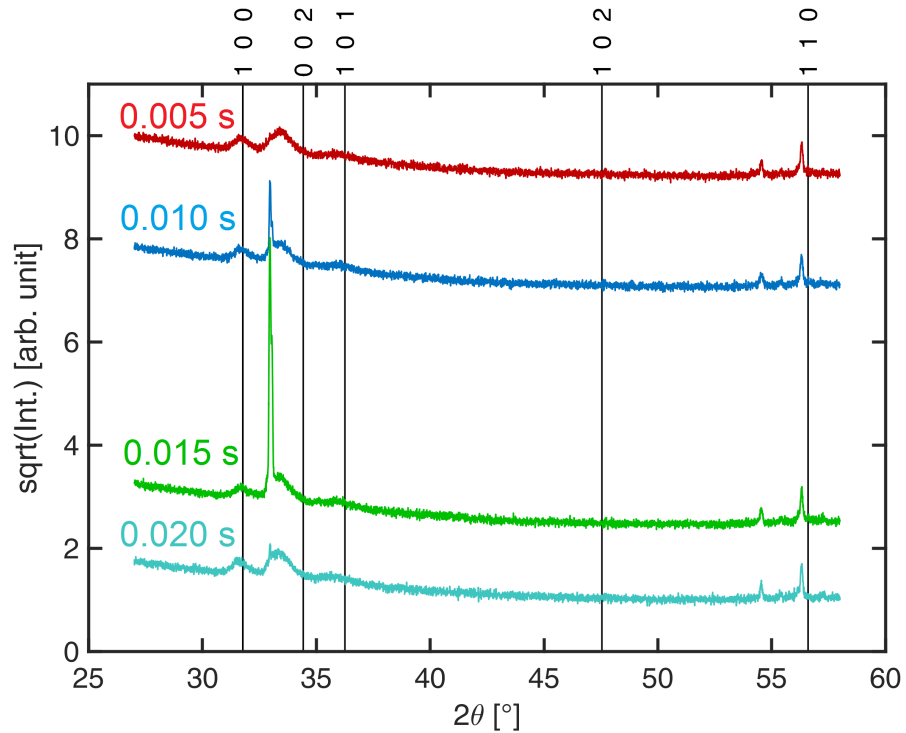


Figure 22:  $\theta/2\theta$ -scan of ZnO films deposited with different DEZ doses. Black Lines show the peak position of a ZnO reference measurement (ICSD-26170) [24].

### 9.2 PLASMA DOSE

In Figure 23 the growth per cycle depending on the DEZ dose is shown. The deposition parameters can be seen in Table 4. The GPC increases with the raising plasma dose and reaches saturation after 7

s of plasma exposure. Below this exposure time the plasma exposure time is too short to oxidise all surface species.

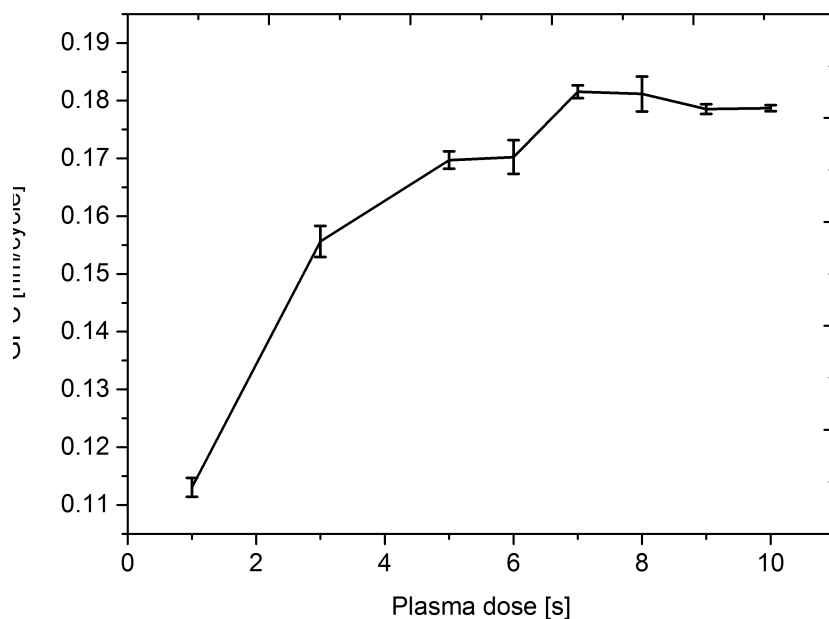


Figure 23: Growth saturation curve by varying the O<sub>2</sub>-plasma dose. The line serves as guide to the eye.

### 9.3 PURGE AFTER DEZ DOSE

In Figure 25 the growth per cycle depending on the purging time after the DEZ dose is shown. The deposition parameters are listed in Table 5. The GPC decreases by increasing the time of purging and saturation is obtained after a purging time of 10 s. For purging times below 10 s not all excess precursor molecules are removed and they could react with co-reactant molecules, which leads to an undesired CVD-component.

At this point it has to be mentioned that after this purging step the program waits 10 s in order to guarantee a stable O<sub>2</sub>-flow. This time is not added to the definition of the purging time after the DEZ dose, since here only the time where argon is flowing is taken into account.

### 9.4 PURGE AFTER PLASMA DOSE

In Figure 25 the growth per cycle depending on the purging time after the plasma dose is shown. The deposition parameters are listed in Table 5. With increasing purging times the GPC decreases and saturates at a plasma purging time of 25 s. For purging times below 25 s not all excess oxidising species are removed and they could react

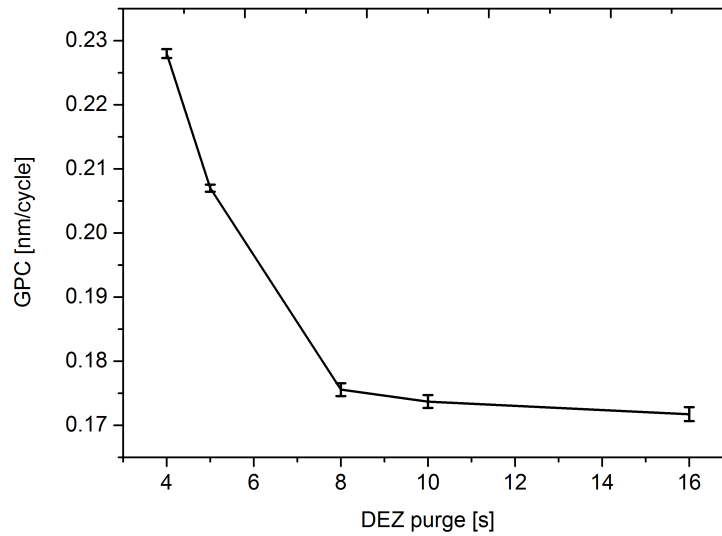


Figure 24: Growth saturation curve by varying the purging time after the DEZ dose. The line serves as guide to the eye.

with the DEZ during the precursor step, which leads to an undesired CVD-component.

#### 9.4.1 XRD measurements

In Figure 22 the  $\theta/2\theta$ -scan of ZnO films deposited with different purging times after the plasma dose can be seen. In all samples the (100) and the (101) peak of the ZnO reference measurement appear without any significant deviation.

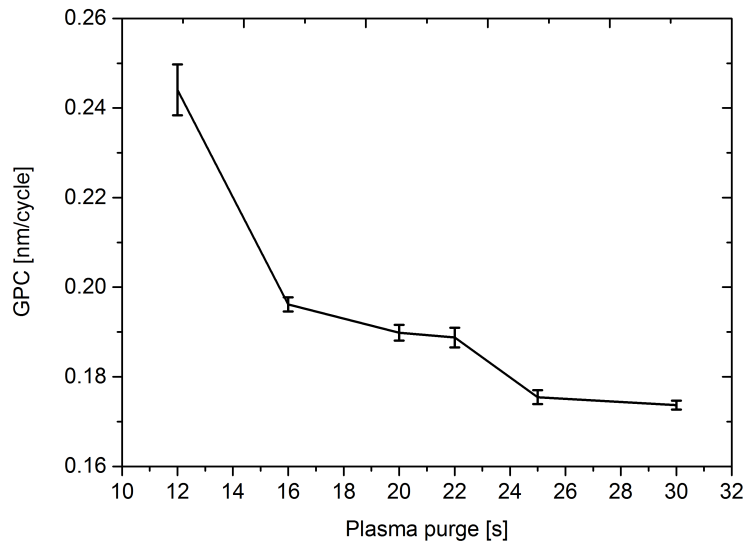


Figure 25: Growth saturation curve by varying the purging time after the plasma dose. The line serves as guide to the eye.

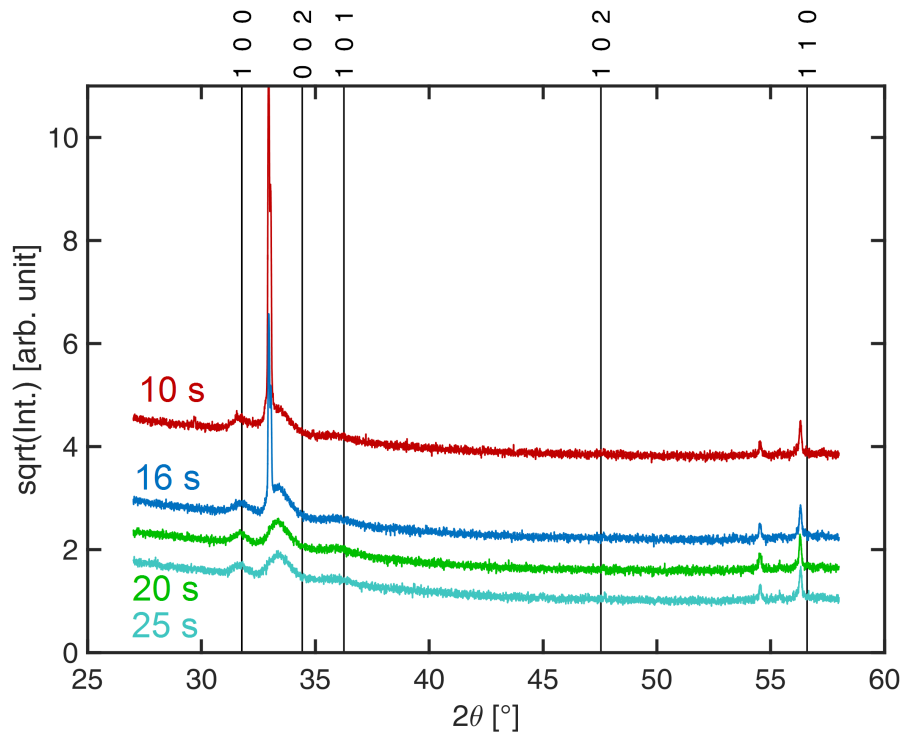


Figure 26:  $\theta/2\theta$ -scan of ZnO films deposited with different times of purging after the plasma dose. Black Lines show the peak position of a ZnO reference measurement (ICSD-26170) [24].

## 9.5 OPTIMUM RECIPE

With the optimum values of all four steps of the ALD-cycle the optimum recipe is obtained and is listed in Table 8. The GPC is 1.8 Å/cycle, which is comparable to literature values and values before the reconditioning of the system.

Table 8: Optimum recipe

| DEZ DOSE / s | PURGE / s | PLASMA DOSE / s | PURGE / s |
|--------------|-----------|-----------------|-----------|
| 0.015        | 12        | 8               | 28        |

### 9.5.1 XRD measurements

An XRD-measurement of ZnO on a Si-substrate, deposited under the optimum conditions, should demonstrate that the crystalline structure is exactly the same as before the reconditioning of the reactor. In Figure 27 the  $\theta/2\theta$ -scan of ZnO films, deposited with the optimum recipe under old and new reactor conditions, can be seen. Under the old reactor conditions in all samples the (100) and the (101) peak of the ZnO reference measurement appear without any significant deviation. A preferential orientation in the (100) direction can be determined. The  $\theta/2\theta$ -scan of the sample, which was deposited with ZnO under the current reactor conditions, shows exactly the same peaks.

### 9.5.2 FTIR measurement

In order to investigate that the contaminations of Carbon in the ZnO film, deposited with the new optimum recipe, a FTIR measurement is performed.

Figure 28 shows the transmittance spectrum of a ZnO film prepared under the conditions of the optimum recipe. The peak at around  $2400\text{ cm}^{-1}$  refers to the  $\text{CO}_2$  bending, which is used for purging the measurement environment. The peak at  $1113\text{ cm}^{-1}$  shows the Si-O bending and is positive because of the reference measurement of a pristine Si-substrate. At  $525\text{ cm}^{-1}$  the Zn-O stretching is shown. The peak at  $1100\text{ cm}^{-1}$  shows that there are still small Carbon impurities in the ZnO layer. That result corresponds with the results in the thesis of Julian Pilz [17].

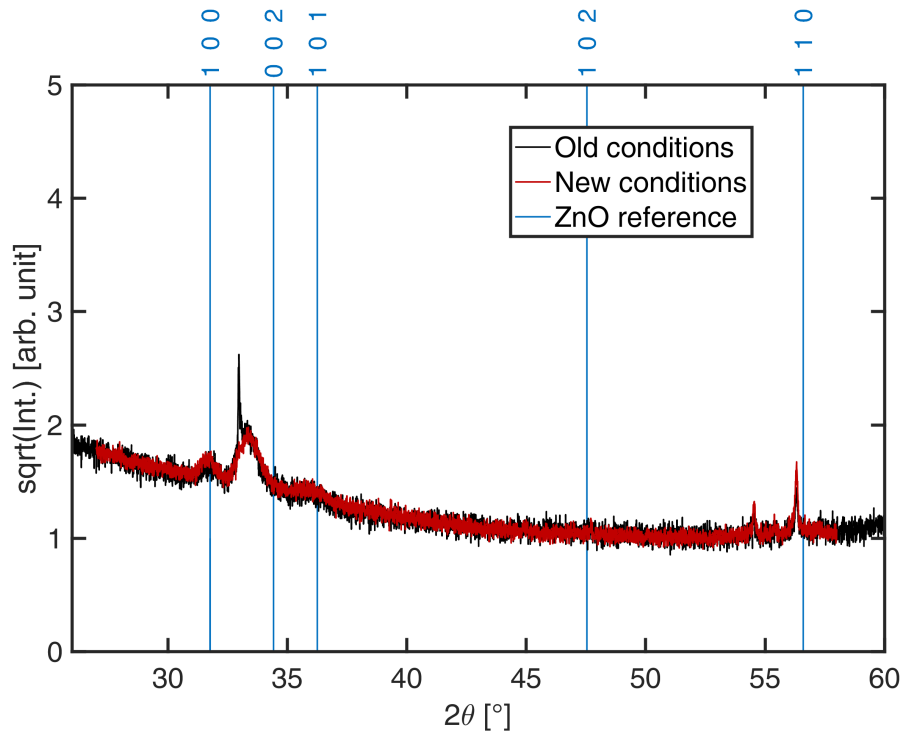


Figure 27:  $\theta/2\theta$ -scan of ZnO films deposited with the optimum recipe under new and old reactor conditions. Blue Lines show the peak position of a ZnO reference measurement (ICSD-26170) [24]. Measurement from old conditions were taken by Julian Pilz.

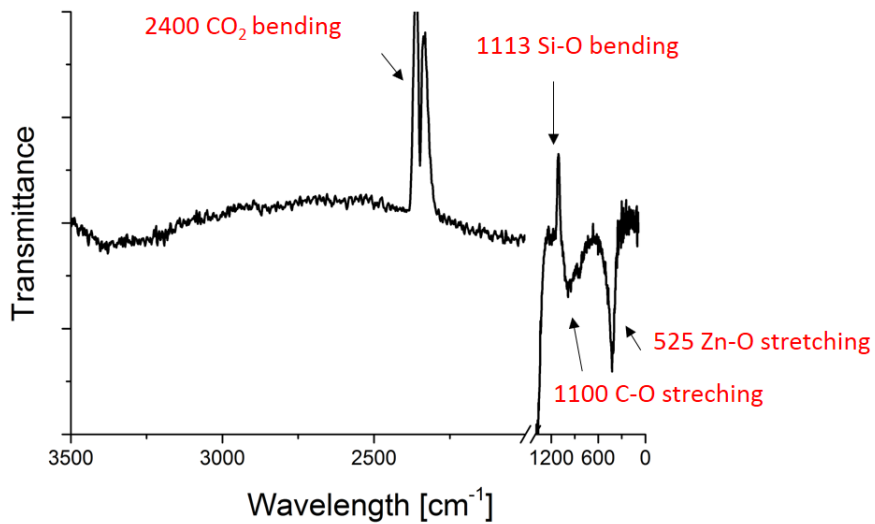


Figure 28: FTIR transmittance spectrum of double-polished Si-wafers deposited with ZnO with the optimum recipe.



## SHADOW MASK LITHOGRAPHY

---

With the optimum ALD recipe first trials in the combination of ALD and lithography are done and the results are described in this chapter.

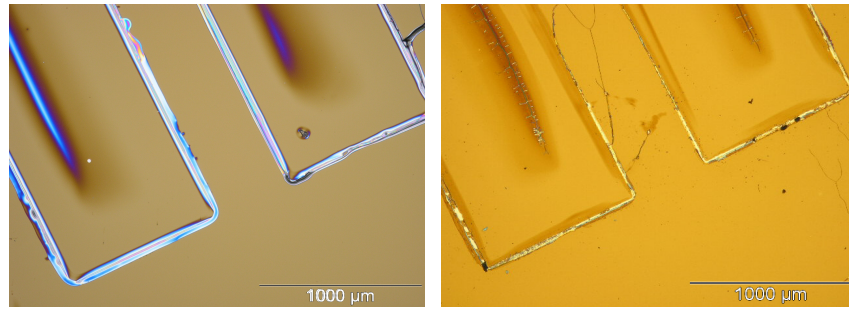
### 10.1 ANALYSIS OF THE LIFT-OFF BY OPTICAL MICROSCOPY

The structure the template gave is big enough for investigations with the optical microscope. In Figure 29a the structure of PVA with deposited ZnO on top can be seen. In Figure 29b one can identify the progressive lift-off after a 20 min soaking in deionized water. Figure 29c shows the state of the sample after another 40 min of lift-off in deionized water, this time strengthened by ultra-sonic bath.

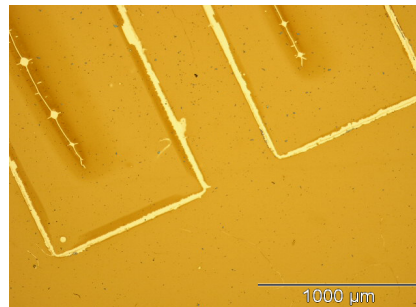
On the borders of the structure the removal works best, since there is the largest gathering of the watersoluble PVA. In between the PVA structures, but also at the position of the PVA before the lift-off, the ZnO seems to remain. The reason for this lies in the big area, which should be lifted off. The ZnO on top is not washed away, but simply touches down on the substrate after the PVA is gone.

### 10.2 SPECTROSCOPIC ELLIPSOMETRY OF DIRECT LITHOGRAPHY SAMPLE

Figure 30 shows the resulting structure of the trial with the mask directly in the reactor during the deposition of zinc oxide. At first sight the structure seems conformal and precise. But an SE measurement of the layer-thickness reveals, that the ZnO is also deposited underneath the template. Figure 30 provides the results of the ellipsometer measurements. It is shown that underneath the template 20 nm of ZnO are deposited. On the areas where the template did not cover the substrate, 42 nm of ZnO were deposited. The cause for this is the uniformity and conformality of the ALD process. For this reason, this method of structuring is unusable.



(a) Sample with structured PVA and ZnO on top (b) Sample after 20 min lift-off in deionized water



(c) Sample after 40 min lift-off in deionized water, strengthened by an ultrasonic bath

Figure 29: Process of lift-off with PVA.

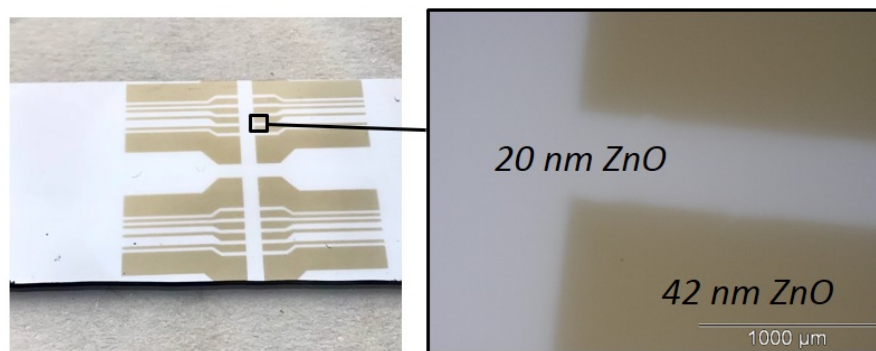


Figure 30: Structure of ZnO after direct lithography. Right picture: The brighter region was covered with a template and is still deposited with ZnO.

## ELECTRON BEAM LITHOGRAPHY

In this chapter the results combining EBL and ALD are shown and the suitability of the EBL process for nanostructuring zinc oxide is reviewed.

## 11.1 ATOMIC FORCE MICROSCOPY

Before depositing ZnO on the structured PMMA, the surface is investigated by AFM imaging. In Figure 31a and 31b the structure after EBL and before ALD is shown. Figure 31c and 31d represent the structure of the EBL pattern after the deposition of ZnO. One can easily recognize the squared pattern, which is filled up with the ZnO. Nevertheless, the structure remains after the ZnO is deposited on top of the PMMA.

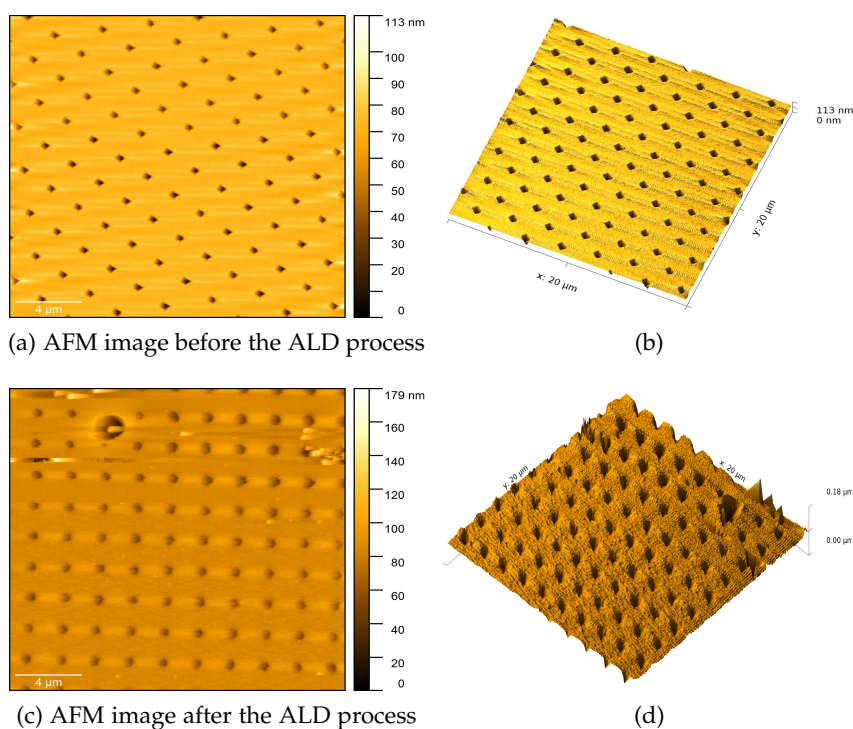


Figure 31: AFM image of the EBL samples before and after the ALD process.

## 11.2 SCANNING ELECTRON MICROSCOPY

In order to control the lift-off process of PMMA in acetone, the samples are investigated by SEM after every 30 min. In Figure 32 the progressive removal of the PMMA is shown for the starred pattern. Step by step the original form of the stars returns. After two hours the difficult pattern is partially uncovered, afterwards the result does not change anymore.

For the squared pattern, the progress after every lift-off step in Figure 33 is more difficult to recognize. One can see that the area surrounding the squares gets rougher and rougher, which is an indicator for the removed PMMA.

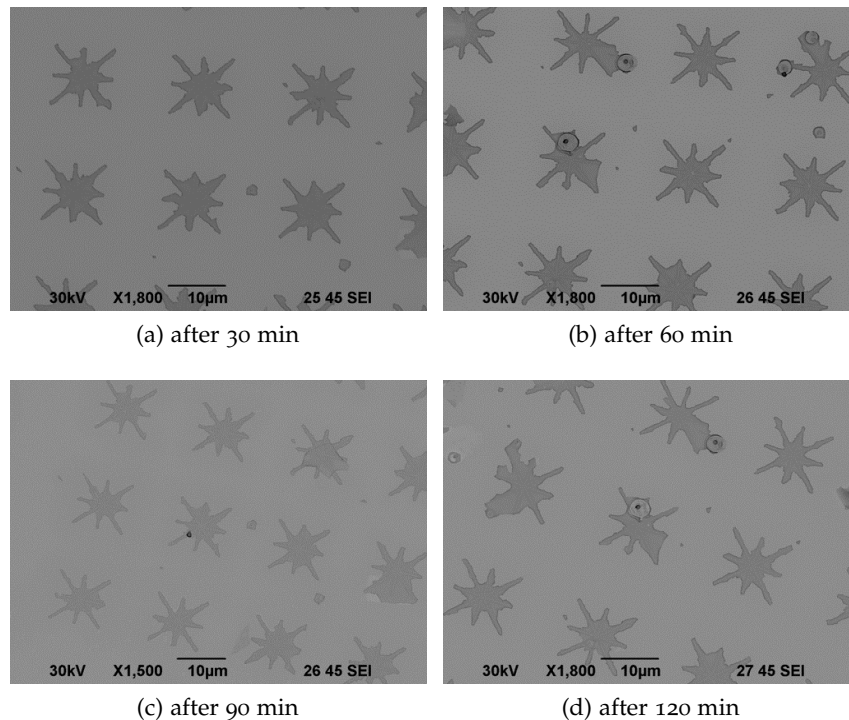


Figure 32: SEM images of starred pattern during the lift-off process. For better recognizability the colors are inverted.

This behaviour has two explanations. One option is that the lift-off process has not worked properly, due to the equipment or the handling. Another option is, that the ZnO grows on the polymer in a way, that it cannot be separated accurately.

## 11.3 EXAMINATION OF THE LIFT-OFF

To verify that the thesis of the lift-off works out under the conditions, which are discussed in Section 11.2, the lift-off behaviour of three different samples is investigated.

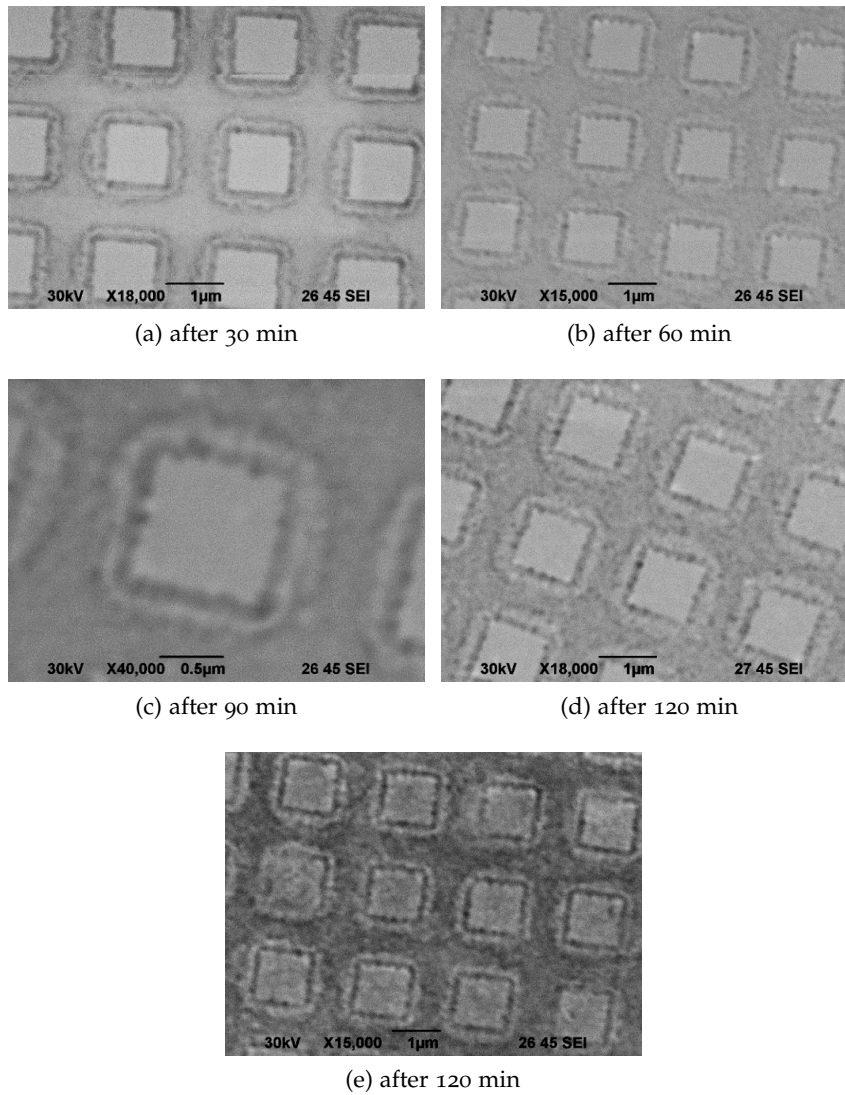


Figure 33: SEM images of squared pattern during the lift-off process. For better recognizability the colors are inverted.

For this purpose, a substrate with a layer of PMMA spincoated onto it and one pristine substrate are deposited under optimum conditions by ALD with zinc oxide. The third sample represents a substrate with only PMMA on it. Figure 34 presents a schematic of the three samples. With ellipsometry the different layer-thicknesses of the three samples are measured and listed in Table 9.

Then each sample undergoes the lift-off procedure, as described in Section 7.4, for the duration of 90 min. Following that, the samples are again investigated with ellipsometry. The thicknesses of the layers after the lift-off are listed in Table 9. The layers on sample 34 a and b with PMMA as ground layer are washed away, as expected, whereas sample 34c with a ZnO layer does not react with the solvent and

Table 9: Thicknesses of layers for comparison before and after lift-off

|                       | PMMA   | PMMA + ZNO | ZNO   |
|-----------------------|--------|------------|-------|
| thickness before / nm | 200.11 | 249.52     | 50.11 |
| thickness after / nm  | 1.52   | 1.49       | 49.45 |

remains. It is obvious that the samples show the desired behaviour and thus, the lift-off procedure is successful.

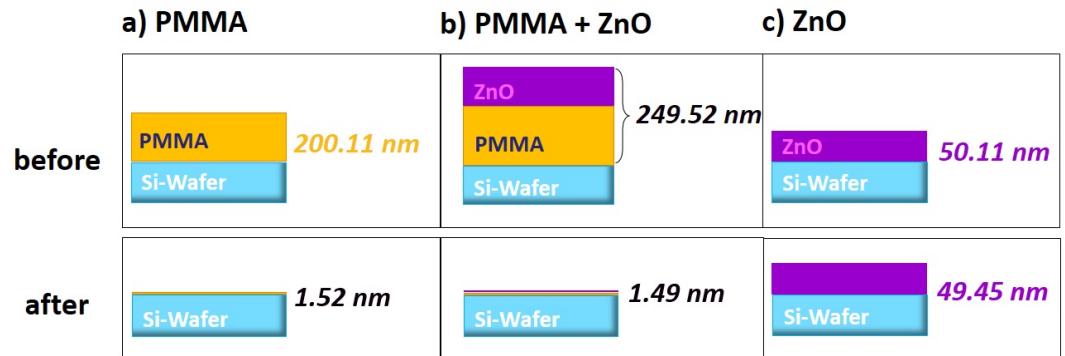


Figure 34: Schematic for the comparison of lift-off behaviour between different coatings before and after the lift-off process. a) Spincoated PMMA on a substrate, b) Spincoated PMMA and ZnO deposited by ALD on top, c) ZnO deposited by ALD on a substrate

## GROWTH OF ZINC OXIDE ON POLYMER

The comparison of the lift-off for three different samples (see Section 11.3) raises the question how the ZnO grows on PMMA. Some polymers are permeable to small molecules of the deposited material on top of them, which leads to the diffusion of the precursor into the bulk material [25].

Suresh et al. [4] established, that for the first 50 cycles of ZnO on PMMA, the growth of zinc oxide was incomplete. For 200 cycles they found a cross-linking behaviour, which is expected to be related to the hydrophilic carbonyl functionality of PMMA, which enables the concentrating of the zinc precursors within the PMMA template.

Through several investigations of samples, which were first spincoated with PMMA and then deposited with zinc oxide under optimum conditions (see Table 8), answers could be found.

## 12.1 ANALYSIS OF ZINC OXIDE ON PMMA BY X-RAY REFLECTIVITY

One way to examine the structure of layers is performing X-ray reflectivity (XRR). XRR is a promising method for non-destructive and quantitative interface characterization.

Before the PMMA-sample is deposited with ZnO, the thickness and the refractive index of PMMA is checked by ellipsometry. For reference measurements of the deposited ZnO, several extra Si-wafers are put in the reactor during the deposition. This enables the measurement of a reference value of ZnO on the Si-substrate by ellipsometry as well. These values are shown in Table 10.

Table 10: Reference values of PMMA and ZnO

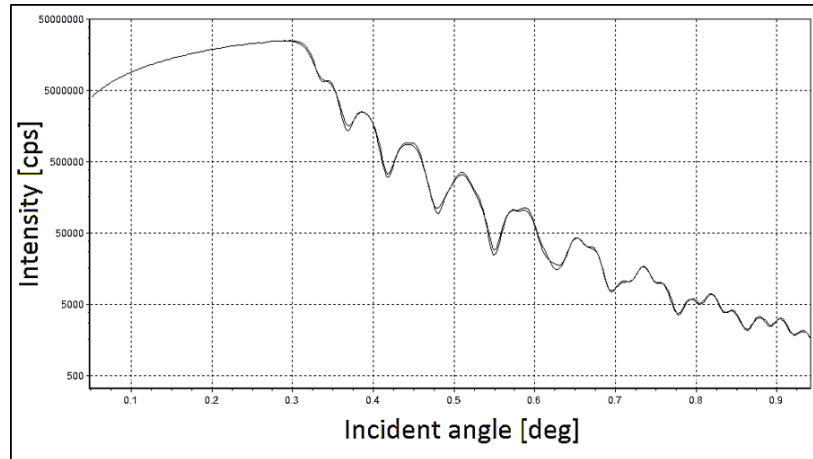
|                  | PMMA   | ZINC OXIDE |
|------------------|--------|------------|
| thickness / nm   | 200.11 | 50.11      |
| refractive index | 1.492  | 1.898      |

With the help of XRR we want to know the exact structure of the layers when ZnO is grown in PMMA.

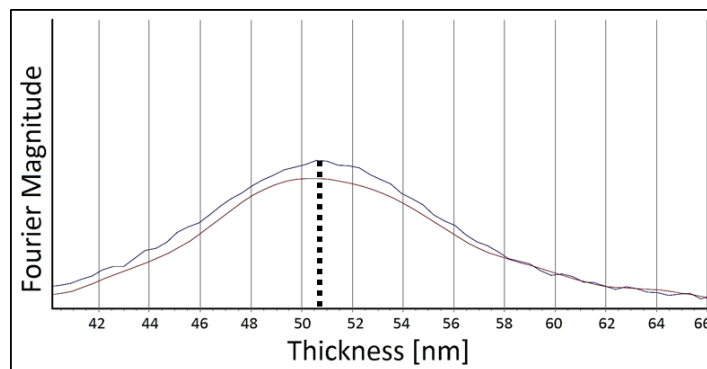
A genetic algorithm is used to process the measurement data. The results show a ZnO thickness of 49.68 nm, which fits the value from the ellipsometry. For the PMMA, a thickness of 140.44 nm is obtained. A kind of interlayer, with a thickness of 10.95 nm, can also be seen.

In Figure 35a the XRR profile for the sample is shown. The oscillations, the so-called Kiessig fringes, give information about the thickness of the layers. Their jagged form provides the information that there are several layers with different densities on the substrate. The fact that the thickness of the PMMA is significantly lower than before the deposition stems from the depth-limitation of the XRR-measurement. The total thickness of the layer is too high to cover for the XRR.

Anyway, the results show us that we are dealing with an interlayer between the zinc oxide and the polymer, instead of a sharp border.



(a) X-ray reflectivity profile for ZnO on PMMA



(b) Fourier transform of the XRR profile.

Figure 35: X-ray reflectivity profiles of ZnO grown on PMMA.

## 12.2 ANALYSIS OF ZINC OXIDE ON PMMA BY SPECTROSCOPIC ELLIPSOMETRY

From the XRR-measurement it is known that the ZnO diffuses into the polymer layer. With spectroscopic ellipsometry and the appropriate software CompleteEASE, an exact model of the layer structure should be determined.

The first trial of fitting the layer structure is a model with two layers,

where a sharp border between the PMMA and the ZnO is assumed. The ZnO and PMMA layer are fitted with a Cauchy model, where the coefficients are calculated by the software. The results in Table 11 show that the individual layers have a lower refractive index than they would have when separated (compare with Table 10). It also seems, that the ZnO is thicker than on the reference Si-wafer, while the PMMA is reduced. That indicates an interlayer as well.

Given this evidence, a model with three layers is fitted. The software is fed with the Cauchy coefficients for PMMA [26], which are set as fixed parameters. The ZnO is fitted with a GenOsc model, to describe the absorption and maintain the Kramers-Kronigs consistency. For the interlayer a Cauchy layer is used, where the coefficients are calculated from the software, since they are unknown (see Figure 36). These results are in accordance with the results of the XRR analysis in Section 12.1. On top of the sample, the model shows a layer of pure ZnO with its appropriate refractive index (see Table 10). Next, there is an interlayer with a refractive index close to the one of ZnO. On the bottom, there is a layer of PMMA with the fitting refractive index.

In literature, ideal masks for ALD are those which show only minimal interaction with the volatile precursors and therefore very small diffusion. Thus, PMMA would not serve as an excellent ALD mask. Nonetheless, PMMA is widely employed as a resist and can be utilized to gain acceptable ALD material patterns [4].

|   |
|---|
| Layer # 4 = <a href="#">ZnO-GenOsc</a> ZnO Thickness = <b>40.56 nm</b> (fit)<br><a href="#">Add Oscillator</a> <a href="#">Show Dialog</a> Fast Gaussian Calc = <a href="#">ON</a><br>Einf_ZnO = <a href="#">1.153</a><br>UV Pole Amp._ZnO = <a href="#">0.000</a> UV Pole En._ZnO = <a href="#">11.000</a><br>IR Pole Amp._ZnO = <a href="#">0.000</a><br><b><a href="#">Fit All</a> <a href="#">Clear All</a> <a href="#">Add Amp.</a> <a href="#">Add Br.</a> <a href="#">Add En.</a></b><br>1: Type = <a href="#">Tauc-Lorentz</a> Amp1_ZnO = <a href="#">41.5800</a><br>Br1_ZnO = <a href="#">0.509</a> Eo1_ZnO = <a href="#">3.573</a> Eg1_ZnO = <a href="#">3.065</a> Common Eg = <a href="#">OFF</a><br>2: Type = <a href="#">Tauc-Lorentz</a> Amp2_ZnO = <a href="#">16.7519</a><br>Br2_ZnO = <a href="#">0.844</a> Eo2_ZnO = <a href="#">8.600</a> Eg2_ZnO = <a href="#">0.0512</a> Common Eg = <a href="#">OFF</a> |
| Layer # 3 = <a href="#">Cauchy</a> Thickness # 3 = <b>9.52 nm</b> (fit)<br>A = <a href="#">1.770</a> (fit) B = <a href="#">0.03609</a> (fit) C = <a href="#">0.0000</a><br>k Amplitude = <a href="#">0.0000</a> Exponent = <a href="#">1.500</a><br>Band Edge = <a href="#">400.0 nm</a>  |
| Layer # 2 = <a href="#">PMMA</a> PMMA Thickness = <b>194.41 nm</b> (fit)<br>A_PMMA = <a href="#">1.488</a> B_PMMA = <a href="#">0.00290</a> C_PMMA = <a href="#">0.00015790</a><br>k Amplitude_PMMA = <a href="#">0.0000</a> Exponent_PMMA = <a href="#">1.500</a><br>Band Edge = <a href="#">400.0 nm</a>  |
| Layer # 1 = <a href="#">NTVE_JAW</a> Native Oxide = <a href="#">1.50 nm</a><br>Substrate = <a href="#">SI_JAW</a>   |

Figure 36: Three layer model from ellipsometer measurement. The data is fitted with the Software Complete EASE.

Table 11: Thicknesses of layers of PMMA and ZnO measured by spectroscopic ellipsometry,  
 t ... thickness in nm  
 n ... refractive index

|               | PMMA   |       | Interlayer |       | ZnO    |       |
|---------------|--------|-------|------------|-------|--------|-------|
|               | t / nm | n     | t / nm     | n     | t / nm | n     |
| 2 layer model | 185.69 | 4.480 | -          | -     | 58.22  | 1.877 |
| 3 layer model | 194.41 | 1.496 | 8.52       | 1.859 | 40.56  | 1.898 |

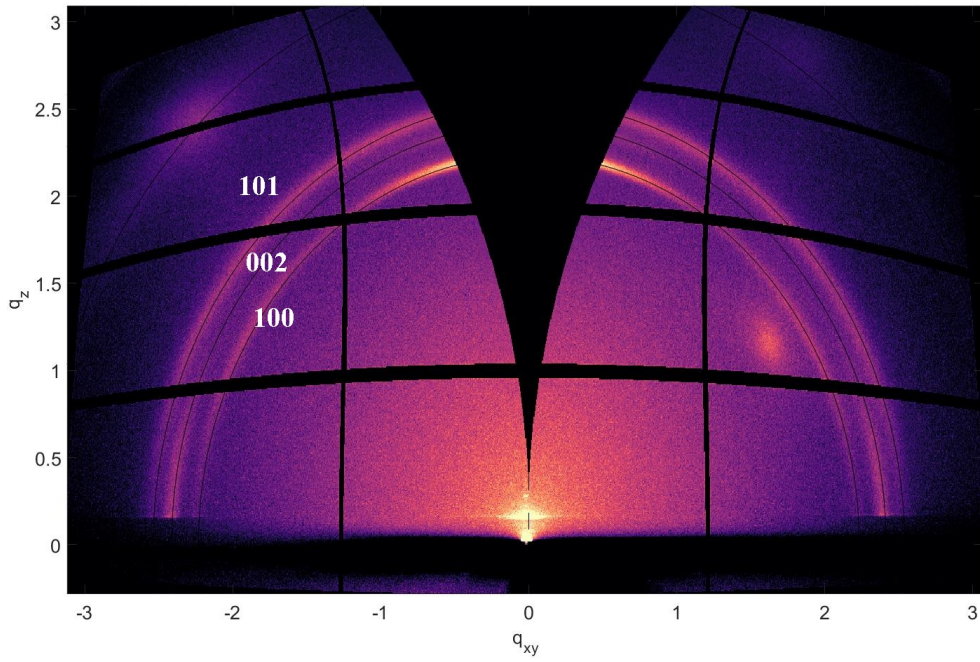
### 12.3 ANALYSIS OF ZINC OXIDE ON PMMA BY X-RAY DIFFRACTION

According to Napari et al. [25] the crystallinity of their ZnO changes when it is deposited on a PMMA substrate. To analyze the crystalline properties of our zinc oxide when it is grown on a polymer, Grazing incidence X-ray diffraction (GIXD) was used. The following measurements were performed at the XRD<sub>1</sub> beamline at Elettra in Trieste.

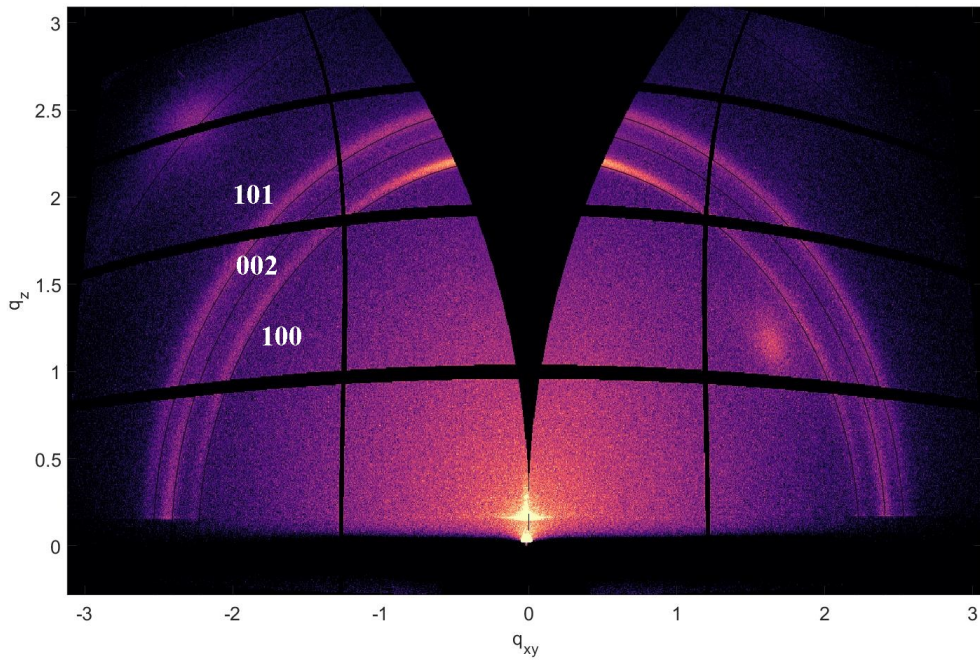
From the XRD measurement in Figure 27 the preferential direction in the (100) direction and the present peak in the (101) direction of the deposited ZnO are known.

Figure 37a shows the GIXD-map of ZnO deposited on a Si-substrate. The sample shows a polycrystalline pattern. The diffraction rings for the (100), (002), and (101) reflection are observed. For the (100) direction the intensity increases towards the specular direction, because the (100) plane is preferred aligned parallel to the substrate. These results agree with the XRD measurements in Section 9.5.1.

Figure 37b shows the GIXD-map of ZnO grown on a polymer. The polycrystalline pattern and the diffraction rings are in accordance with the results of Figure 37a. Therefore one can assume that the ZnO we deposit retains its crystallinity when it is grown on a polymer.



(a) GIXD-map of ZnO on Si-substrate



(b) GIXD-map of ZnO on PMMA

Figure 37: GIXD-map of ZnO grown on a Si-substrate and ZnO grown on a polymer.

## 12.4 GLASS TRANSITION TEMPERATURE MEASUREMENTS

An important characteristic value for amorphous materials like PMMA is the glass transition temperature  $T_g$ . This is the temperature, where the polymer turns from a relatively hard and glassy state into a more viscous one. The  $T_g$  for PMMA is more a range than a value and can be seen in Section 4.2.1.

The idea to measure the  $T_g$  of PMMA under several conditions is to see how the PMMA reacts to the treatment in the reactor during the deposition.

This analysis is done by an ellipsometer-in-situ measurement with a temperature ramp. The stage temperature is linearly raised, starting at 25 °C, going up to 140 °C, where the temperature is held for 10 min and then is cooled down to 25 °C. To ensure the repeatability this is carried out four times (see Figure 38).

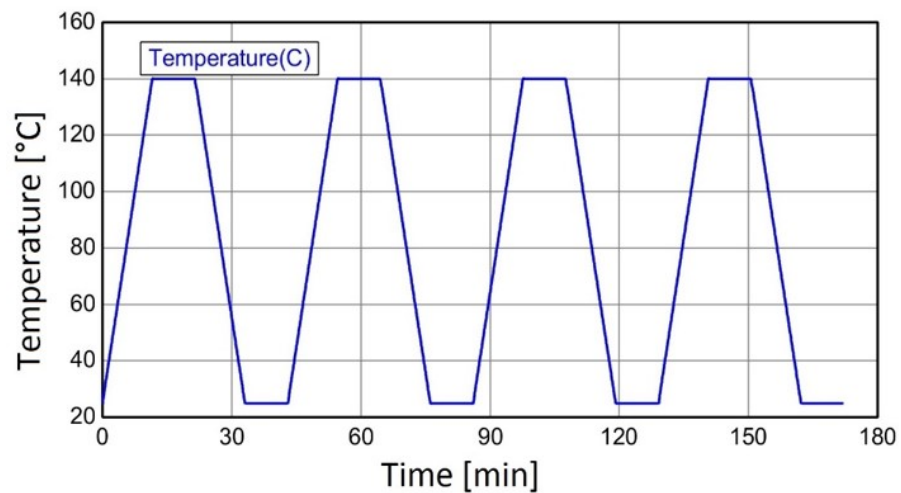


Figure 38: Temperature profile for the measurement of the glass transition temperature.

## 12.4.1 Comparison of PMMA and PMMA with ZnO on top

With the procedure described above, the values for the  $T_g$  for a PMMA layer with a thickness around 200 nm are measured. Afterwards this sample is deposited with ZnO by ALD and the same measurement is done again.

In Figure 39a the  $T_g$  for PMMA can be seen. It is 110 °C, which fits the literature value [15].

The  $T_g$  for PMMA with ZnO on top behaves in a different manner than expected. One would assume the ZnO would harden the polymer and the  $T_g$  would rise. In this measurement the  $T_g$  decreases, but it is, with 95 °C, still within the range.

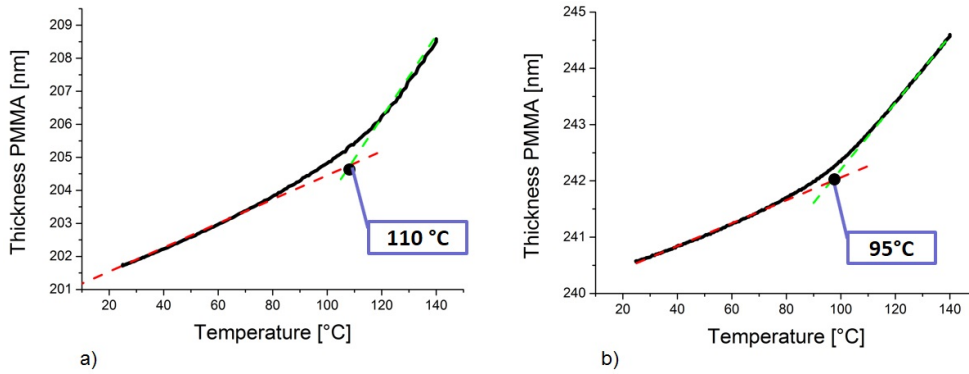


Figure 39: Temperature dependent thickness changes in PMMA and PMMA+ZnO. a)  $T_g$  for PMMA on a Si-substrate, b)  $T_g$  for PMMA on a Si-substrate and ZnO deposited on top. For b) only the PMMA layer is modelled.

12.4.2 Comparison of PMMA and plasma treated PMMA

Since the ZnO on top of the PMMA did not have a big impact on the  $T_g$  of the PMMA, the next step is to examine if the plasma exposure harms the PMMA.

A sample with a PMMA layer with a thickness of around 70 nm is measured with the procedure described above. Afterwards the sample is put into the reactor and treated with plasma for seven cycles. Afterwards the same measurement is done again.

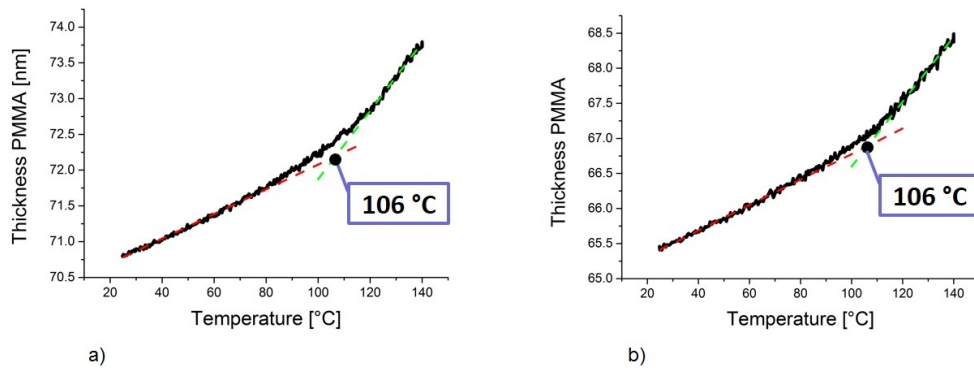


Figure 40: Temperature dependent thickness changes in PMMA and plasma treated PMMA. a)  $T_g$  for PMMA on a Si-substrate, b)  $T_g$  for PMMA on a Si-substrate after plasma treatment in the ALD reactor.

Figure 40a shows the  $T_g = 106$  °C for PMMA. In Figure 40b the  $T_g = 106$  °C for the PMMA after plasma treatment. This excludes that the PMMA is destroyed or changed by the plasma. The behaviour which was observed in Figure 39b must relate to the diffusion of the ZnO into the PMMA.



## CONCLUSION AND OUTLOOK

---

These studies investigate the combination of Atomic Layer Deposition and lithographic techniques and serve as groundwork for further research in the area of nanostructuring materials with the help of ALD. For ideal ALD growth, the optimum dose for each ALD step could be achieved. The optimum recipe is 0.015/12/8/28 s (DEZ dose/purge/-plasma dose/purge), for which a growth per cycle of 1.8 Å is obtained. The crystallinity of the deposited ZnO shows a preferential orientation in the (100) direction.

With shadow mask lithography and PVA first structures of ZnO were received, but not yet in the nanometer range.

Direct lithography with a template directly on the substrate in the reactor confirmed the conformality of the ALD process, since ZnO was also deposited underneath the template. For this reason this method is not suitable for nanostructuring ZnO.

With Electron Beam Lithography, using the positive resist PMMA, nanostructured zinc oxide could be gained. Since the lift-off process did not remove the excess material conformally, the behaviour of ZnO on polymers was further investigated.

It was found out that the ZnO diffuses into the polymer and results in an interlayer. Ellipsometer- and XRR-measurements yielded that the polymer on the very bottom and the ZnO on the very top did not change their crystallinity, nor does their density. The zinc oxide we deposited remained unchanged on the utilized polymers PVA and PMMA.

Next steps could be the usage of area selective ALD. The goal here is to develop techniques for area-selective film growth at the nanometer range, preferably independent of the deposited film thickness. For this purpose, the film growth is limited to certain areas, while in the other parts film growth is avoided. To obtain this selectivity, a substrate is patterned by block copolymers (BCL) or self assembled inerts toward the ALD reactants [4] [27].



## BIBLIOGRAPHY

---

- [1] ERC. *ERC funded projects*. 2015. URL: [https://erc.europa.eu/projects-figures/erc-funded-projects/results?search\\_api\\_views\\_fulltext=coclite](https://erc.europa.eu/projects-figures/erc-funded-projects/results?search_api_views_fulltext=coclite).
- [2] A. J. M. Mackus and W. M. M. Bol A. A. & Kessels. "The use of atomic layer deposition in advanced nanopatterning." In: *Nanoscale* 6.19 (2014), pp. 10941–10960.
- [3] Alexander Christian Pyymaki Perros. "Thermal and plasma-enhanced atomic layer deposition: the study of and employment in various nanotechnology applications." PhD dissertation. Aalto University, School of Electrical Engineering, 2015.
- [4] Vignesh Suresh, Meiyu Stella Huang, M. P. Srinivasan, Cao Guan, and Sivashankar Fan Hong Jin & Krishnamoorthy. "Robust, High-Density Zinc Oxide Nanoarrays by Nanoimprint Lithography-Assisted Area-Selective Atomic Layer Deposition." In: *The Journal of Physical Chemistry* 116.44 (2012), pp. 23729–23734.
- [5] Nicola Pinna and Mato Knez. *Atomic layer deposition of nanostructured materials*. John Wiley & Sons, 2012.
- [6] Cole W. Litton and Thomas C. Reynolds Donald C. & Collins. *Zinc Oxide Materials for Electronic and Optoelectronic Device Applications*. John Wiley & Sons, 2011.
- [7] Hadis Morkoç and Ümit Özgür. *Zinc Oxide: Fundamentals, Materials and Device Technology*. Wiley-VCH Verlag GmbH & Co. KGaA, 2007.
- [8] Vaseem Mohammad and Yoon-Bong Umar Ahmad & Hahn. "ZnO Nanoparticles: Growth, Properties, and Applications." In: vol. 5. *Metal Oxide Nanostructures and Their Applications*. 2010, pp. 1–36.
- [9] H. Lee, K. Y. Yang, S. Hong, and G. Y. Schaper C. D. & Jung. "Nano-imprint Lithography of 100nm sized patterns using water soluble PVA template." In: vol. 121-123. *Diffusion and Defect Data Pt.B: Solid State Phenomena*. 2007, pp. 661–664.
- [10] M. J. Biercuk, D. J. Monsma, C. M. Marcus, and J. S. & Gordon R. G. Becker. "Low-temperature atomic-layer-deposition lift-off method for microelectronic and nanoelectronic applications." In: *Applied Physics Letters* 83.12 (2003), p. 2405.
- [11] Matteo Altissimo. "E-Beam Lithography for Micro-/nanofabrication." In: *Biomicrofluidics* 4.2 (2010), p. 026503.

- [12] Tommi Kääriäinen, David Cameron, Marja-Leena Kääriäinen, and Arthur Sherman. *Atomic layer deposition: principles, characteristics, and nanotechnology applications*. John Wiley & Sons, 2013.
- [13] H. C. M. Knoop, S. E. Potts, and W. M. M. Bol A. A. & Kessels. "Atomic Layer Deposition." In: vol. 3. *Handbook of Crystal Growth: Thin Films and Epitaxy: Second Edition*. 2014, pp. 1101–1134.
- [14] Mato Knez and Lauri Nielsch Kornelius & Niinistö. "Synthesis and Surface Engineering of Complex Nanostructures by Atomic Layer Deposition." In: *Advanced Materials* 19.21 (2007), pp. 3425–3438.
- [15] Polymer Properties Database. *Polymethylacrylates*. 2018. URL: <http://polymerdatabase.com/polymer%20classes/Polymethacrylate%20type.html>.
- [16] J. Krenn. *Electron Beam Lithography*. 2007. URL: [http://nanooptics.uni-graz.at/ol/work/m\\_ebl.html](http://nanooptics.uni-graz.at/ol/work/m_ebl.html).
- [17] BSc Julian Pilz. "Plasma-enhanced atomic layer deposition of zinc oxide thin films." Master's Thesis. Graz University of Technology, 2017.
- [18] Triratna Muneshwar, Gem Shoute, Doug Barlage, and Ken Cadien. "Plasma enhanced atomic layer deposition of ZnO with diethyl zinc and oxygen plasma: Effect of precursor decomposition." In: *Journal of Vacuum Science & Technology A: Vacuum, Surfaces, and Films* 34.5 (2016), p. 050605.
- [19] J. A. Woollam. *Ellipsometry Measurements*. 2017. URL: <http://www.jawoollam.com/resources/ellipsometry-tutorial/ellipsometry-measurements>.
- [20] J. A. Woollam. *CompleteEASE Data Analysis Manual*. 2008. URL: [https://crn2.3it.usherbrooke.ca/guide\\_sb/appareils/Ellipsometre/CompleteEASE%20Manual.pdf](https://crn2.3it.usherbrooke.ca/guide_sb/appareils/Ellipsometre/CompleteEASE%20Manual.pdf).
- [21] Mario Birkholz. *Thin film analysis by X-ray scattering*. John Wiley & Sons, 2006.
- [22] Shigesaburo Ogawa and Isao Takahashi. "Glass Transition of Ultrathin Sugar Films Probed by X-Ray Reflectivity." In: *Carbohydrate*. InTech, 2017. Chap. 06.
- [23] Philip Anu, Thomas Subin, and Kumar K Rajeev. "Calculation of growth per cycle (GPC) of atomic layer deposited aluminium oxide nanolayers and dependence of GPC on surface OH concentration." In: *Pramana, Journal of Physics* 82.3 (2014), pp. 563–569.

- [24] SC Abrahams and JL Bernstein. "Remeasurement of the structure of hexagonal ZnO." In: *Acta Crystallographica Section B: Structural Crystallography and Crystal Chemistry* 25.7 (1969), pp. 1233–1236.
- [25] M. Napari, J. Malm, R. Lehto, J. Julin, K. Arstila, and M. Sajavaara T. & Lahtinen. "Nucleation and growth of ZnO on PMMA by low-temperature atomic layer deposition." In: *Journal of Vacuum Science & Technology A* 33.1 (2015). AVS, 01A128.
- [26] Mikhail Polyanskiy. *Optical constants of PMMA resists*. 2018. URL: [https://refractiveindex.info/?shelf=other&book=pmma\\_resists&page=Microchem950](https://refractiveindex.info/?shelf=other&book=pmma_resists&page=Microchem950).
- [27] Robin H. A. Ras, Elina Sahramo, Jari Malm, and Maarit Raula Janne & Karppinen. "Blocking the Lateral Film Growth at the Nanoscale in Area-Selective Atomic Layer Deposition." In: *American Chemical Society* 130.34 (2008), 11252–11253.